COMPUTATIONAL AND THEORETICAL STUDY

OF CELL SENSING AND MIGRATION

A Dissertation

Submitted to the Faculty

of

Purdue University

by

Julien Varennes

In Partial Fulfillment of the

Requirements for the Degree

of

Doctor of Philosophy

May 2018

Purdue University

West Lafayette, Indiana

I dedicate this to all my homies out there.

ACKNOWLEDGMENTS

I would like to thank my advisory and my committee.

TABLE OF CONTENTS

LIST OF TABLES

LIST OF FIGURES

ABSTRACT

Varennes, Julien PhD, Purdue University, May 2018. Computational and Theoretical Study of Cell Sensing and Migration. Major Professor: Andrew Mugler.

Collective cell migration in response to a chemical cue requires both multicellular sensing of chemical gradients and coordinated mechanical action. Examples from morphogenesis and cancer metastasis demonstrate that clusters of migratory cells are extremely sensitive, responding to gradients of less than 1% difference in chemical concentration across a cell body. While the limits to multicellular sensing are becoming known, how this information leads to coherent migration remains poorly understood. We develop a model of multicellular sensing and migration in which groups of cells collectively measure noisy chemical gradients. The output of the sensing process is coupled to individual cells polarization to model migratory behavior. Through the use of numerical simulations, we find that larger clusters of cells detect the gradient direction with higher precision and thus achieve stronger polarization bias, but larger clusters are also accompanied by less coherent collective motion. The trade-off between these two effects leads to an optimally efficient cluster size. Experimental tests of our model are ongoing and are focused on observations of breast cancer cell migration. Future plans include extending the model to systems of cells which include leading-edge cells that are phenotypically different from non-leading cells, and exploring an alternative model of collective migration in which cells make independent measurements and coordinated behavior emerges through local interactions. By completing these studies we aim to understand the precise roles of multicellular sensing in producing collective cell migration, in metastasis and in general.

1. PHYSICAL LIMITS TO MULTICELLULAR SENSING

Cells gather information about their environment by sensing chemical concentrations and concentration gradients. In fact, cells can do this with remarkable precision. The amoeba *Dictyostelium discoideum* is sensitive to differences on the order of ten molecules between its front and back half [1]. It is therefore natural to ask how well cells can sense their environment, and whether the error in the sensing capabilities can be quantified. These questions were first answered by Berg and Purcell almost 40 years ago [2]. They considered a simplified model of a cell in order to calculate a lower limit on the relative error in its measurement of a chemical concentration, and they also showed that the sensory machinery of the *Escheria coli* bacterium operates very near this physical bound. The question of how well single cells measure chemical concentrations has been revisited to account for binding kinetics, spatiotemporal correlations and spatial confinement [3–5]. These studies have helped shape our understanding of how cells sense their environment. However, in nature cells are rarely found alone, and the interactions between nearby cells may alter cells' sensory capabilities.

In many biological contexts cells act in close proximity to one another so their interactions may not be easily ignored when trying to understand the physical limits to sensing. In fact, these interactions can enhance cell sensitivity to the environment. Using communication, clusters of mammary epithelial cells can detect chemical gradients that single cells cannot [6], and cultures of neurons have been shown to be sensitive to single molecule differences across an individual neuron's axonal growth cone [7]. In studying multicellular sensing of chemical concentrations and gradients it is important to recognize that in order to collect these spatially separated measurements from individual cells the information must be communicated to some common location. Explaining how cells efficiently communicate information has been the topic

of recent research. Similar to the limits set by Berg and Purcell, the physical limits to communicated, collective gradient sensing have been derived [6, 8] by using a multicellular version of the local excitation-global inhibition (LEGI) communication model [9], one of the simplest adaptive mechanisms of gradient sensing. With these studies the physical limits of cell sensing have been extended from single cells to multicellular collectives.

In parallel to studies on collective sensing, much recent work has focused on collective cell behavior, including migration. For example, processes in development, cellular migration, pathogenic response, and cancer progression all involve many cells acting in a coordinated way [10–14]. Work has been done in studying how these multicellular systems behave from a mechanical perspective. Simple mechanical models have successfully explained observed collective behaviors such as cell streaming, cell sorting, cell sheet migration, wound healing, and cell aggregation [15–18]. Though these studies accurately model some form of collective cell migration they fail to include the affects of multicellular sensing in driving the mechanics at play. In many biological systems, cells are capable of communicating with one another, so understanding how these cells translate that information into mechanical action is of prime interest.

Here we focus our attention on collective cell migration and how cells use multicellular communication to direct their motion. As summarized, much is known regarding multicellular communication and its physical limits as well as how to model the mechanics of collective behavior. The connection between these two fields, however, is missing. The primary goal of this research is to connect the studies of the physical limits of cell communication to those of cellular dynamics in order to gain deeper insight into collective behavior. These two fields can be connected by creating a model which links the collective sensing output to the polarization of migrating cells. Furthermore, by creating numerical simulations of collective sensing and migration we can relate our model to real biological systems.

One multicellular system of particular interest is that of cancer metastasis. The first step in metastasis is the invasion of tumor cells into the surrounding micro-environment. Invasion is known to occur in a highly organized manner that likely involves communication [13, 14, 19]. Recent work shows that tumor cell invasion is guided by sensory cues to blood vessels and to lymphatics, and that cancer cells can sense their environment with remarkable precision [20]. It is clear that the early stages of metastasis depend on cell sensing and in certain types of cancer, occur in a collective manner. Hence understanding how the limits of multicellular sensing affect collective cell migration can help us better understand how collective tumor cell invasion occurs.

In conjunction with the development and analysis of a model of collective sensing and migration, work with experimental collaborators will help verify whether the proposed model can indeed reproduce experimental results. In developing any theoretical model it is important to be able to validate or disprove the model through experiments. This will be achieved through our collaboration with Professor Bumsoo Han of Purdue University and his research group, who will observe how breast cancer cells migrate in the presence of a chemoattractant gradient. Developing a theoretical model alongside experiment will enable us to verify its accuracy and also match theoretical parameters with experimental observables in order to extend the model to more biological systems.

REVIEW STARTS BELOW

Metastasis is one of the most intensely studied stages of cancer progression because it is the most deadly stage of cancer. The first step of metastasis is invasion, wherein cells break away from the tumor and invade the surrounding tissue. Our understanding of metastatic invasion has benefited tremendously from genetic and biochemical approaches [21–23]. However, the physical aspects of metastatic invasion are still unclear [23]. We know that at a fundamental level, metastatic invasion is a physical process. Tumor cells sense and respond to chemical gradients provided by surrounding cells [20, 24–26] or other features of the tumor environment [20, 27, 28]

(Fig. 2.1A). Indeed, tumor cells are highly sensitive, able to detect a 1% difference in concentration across the cell length [20]. Sensing is ultimately a physical phenomenon. Therefore, can we build a simple physical theory to understand the sensory behavior of tumor cells, and can this physical theory inform treatment options?

Metastatic invasion involves coordinated migration of tumor cells away from the tumor site. In many types of cancer, migration is collective and highly organized, involving the coherent motion of connected groups of cells [13, 19, 26, 29] (Fig. 2.1B). Collective migration is ultimately a physical phenomenon, since it relies on mechanical coupling and can often be understood as emerging from simple physical interactions at the cell-to-cell level. Can we understand the collective migration of tumor cells with simple physical models?

Here we review recent progress on modeling sensing and migration in cells and cell collectives. We discuss metastatic cells explicitly, and emphasize that physical insights gained from other cellular systems can inform our understanding of metastatic invasion. We focus on simple physical models and order-of-magnitude numerical estimates in order to quantitatively probe the extent of, and the limits to, cell sensory and migratory behavior. Our hope is that a more quantitative understanding of metastatic invasion will inform treatment protocols, and to that end we conclude by discussing drug sensitivity and potential treatment strategies (Fig. 2.1C).

1.1 Physical limits to sensory precision

Tumor cells sense very small concentration gradients [20] and act in a collective manner [13, 19, 26, 29]. Here we review the basic theory of concentration and gradient sensing by cells and cell collectives. This theory places physical bounds on sensory precision and allows us to quantitatively compare the capabilities of tumor cells to other cell types.
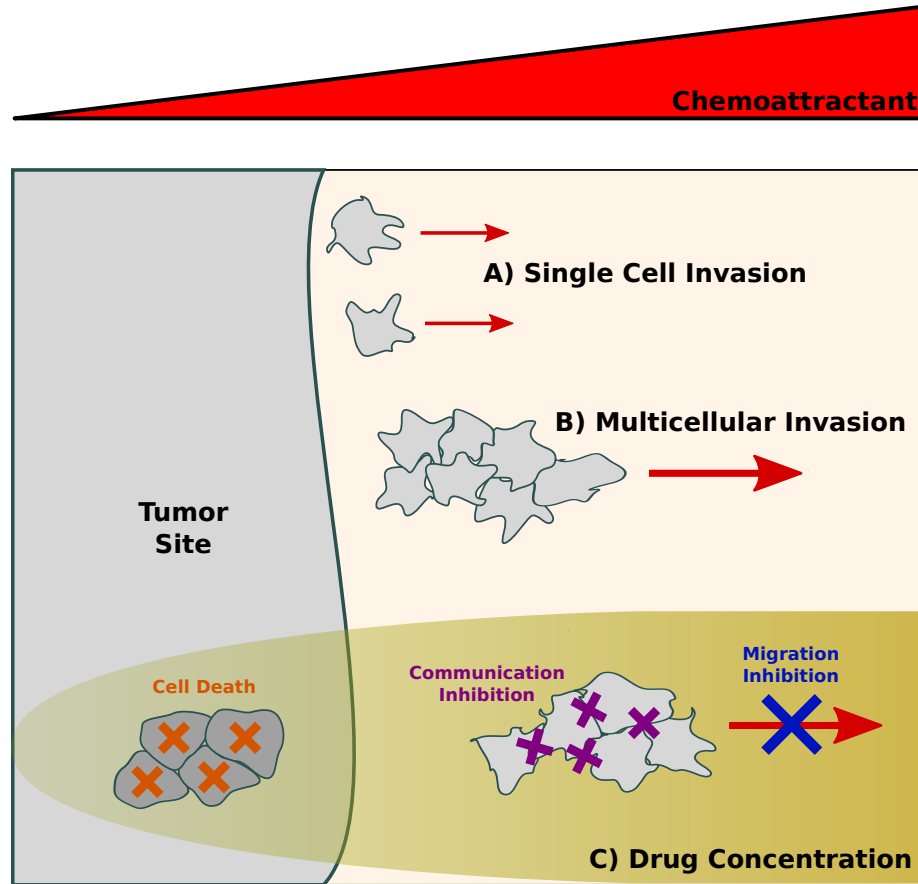
Fig. 1.1. Metastatic invasion is guided by chemical attractants and can occur via (A) single cells or (B) multicellular groups. (C) Drugs are delivered to the tumor environment in order to prevent tumor growth and metastasis. Drugs may cause cell death (orange), block cell-to-cell communication (purple), or prevent cell migration (blue).

1.1.1 Single-cell concentration sensing

Theoretical limits to the precision of concentration sensing were first introduced by Berg and Purcell almost 40 years ago [2]. Berg and Purcell began by considering an idealized cell that acts as a perfect counting instrument. Their simplest model assumed that the cell is a sphere in which molecules can freely diffuse in and out (Fig. 2.2A). The concentration of these molecules is uniform in space, and the cell derives all its information about the concentration by counting each molecule inside
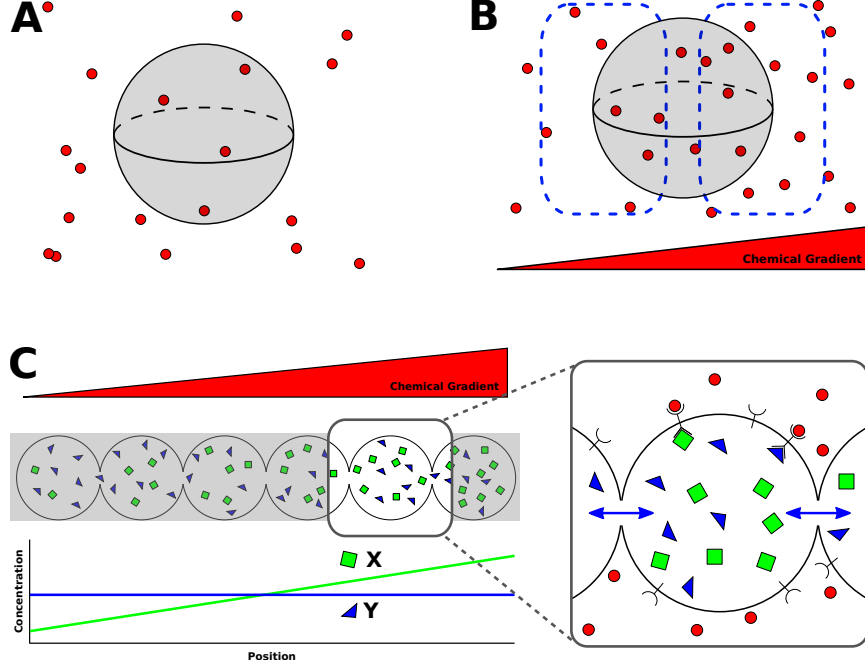
Fig. 1.2. (A) An idealized cell as a permeable sphere that counts molecules inside its volume. (B) A cell counts molecules in two compartments in order to estimate a concentration gradient. (C) The local excitation–global inhibition (LEGI) model of multicellular gradient sensing. Y molecules diffuse between neighboring cells, whereas X molecules do not. The difference between X and Y counts in a given cell reports the extent to which that cell's concentration measurements are above the average.

its spherical body. The expected count is $\bar{n} = \bar{c}V$ where $\bar{c}$ is the mean concentration and V is the cell volume. However, since molecules arrive and leave via diffusion, there will be fluctuations around this expected value. Diffusion is a Poisson process, meaning that the variance in this count σ_n^2 equals the mean $\bar{n}$. Therefore the relative error in the cell's concentration estimate is $\sigma_c/\bar{c} = \sigma_n/\bar{n} = 1/\sqrt{\bar{c}V}$.

The cell can improve upon the relative error in its concentration estimate by time-averaging over multiple measurements. However, consecutive measurements are only statistically independent if they are separated by a sufficient amount of time such that the molecules inside the cell volume are refreshed. The amount of time required

is characterized by the diffusion time, $\tau \sim V^{2/3}/D \sim a^2/D$, where D is the diffusion constant and a is the cell diameter. In a time period T the cell makes $\nu = T/\tau$ independent measurements, and the variance is reduced by the factor $1/\nu$. This gives the long-standing lower limit

$$\frac{\sigma_c}{\bar{c}} = \frac{\sigma_n}{\bar{n}} \sim \frac{1}{\sqrt{a\bar{c}DT}} \tag{1.1}$$

for the cell's relative error in estimating a uniform concentration. The relative error decreases with a and $\bar{c}$, since the molecule count is larger, and also with D and T, since more independent measurements can be made. Berg and Purcell derived this limit more rigorously [2], and the problem has been revisited more recently to account for binding kinetics, spatiotemporal correlations, and spatial confinement [3–5]. In all cases a term of the form in Eq. 2.1 emerges as the fundamental limit for three-dimensional diffusion.

Do cells reach this limit? Berg and Purcell themselves asked this question in the context of several single-celled organisms, including the *Escheria coli* bacterium [2]. Motility of *E. coli* has two distinct phases: the run phase in which a cell swims in a fixed direction, and the tumble phase in which the cell erratically rotates in order to begin a new run in a different direction. The bacterium biases its motion by continually measuring the chemoattractant concentration, and extending the time of runs for which the change in concentration is positive [2,30]. The change in concentration $\Delta\bar{c} = Tv\bar{g}$ over a run time T depends on the concentration gradient $\bar{g} = \partial\bar{c}/\partial x$ and the bacterium's velocity v. Berg and Purcell argued that for a change in concentration to be detectable, it must be larger than the measurement uncertainty, $\Delta\bar{c} > \sigma_c$. Together with Eq. 2.1, this places a lower limit on the run time, $T > [\bar{c}/(aDv^2\bar{g}^2)]^{1/3}$. Using typical values [2] for the sensory threshold of *E. coli* of $\bar{c} = 1$ mM, $\partial\bar{c}/\partial x = 1$ mM/cm, $a = 1$ μm, $v = 15$ μm/s, and $D = 10^{-5}$ cm^2/s, we find $T > 0.1$ s. Actual run times are on the order of 1 s. Thus we see that *E. coli* chemotaxis is consistent with this physical bound. The fact that actual run times are not too much longer than the minimum indicates that the sensory machinery of *E. coli* operates near the optimal precision of a perfect counting device. If *E. coli* were to use much shorter run

times, there would be no way to acquire sufficient statistics, and chemotaxis would be physically impossible.

1.1.2 Single-cell gradient sensing

Unlike *E. coli*, larger cells like tumor cells do not need to swim to detect gradients. Larger cells, including amoeba, epithelial cells, neutrophils, and neurons, sense gradients by comparing concentrations between compartments in different locations of the cell body [31]. These compartments are typically receptors or groups of receptors on the cell surface, but in a simple model we may treat these compartments as idealized counting volumes as we did before (Fig. 2.2B). The difference in counts between two such compartments provides the cell with an estimate of the gradient. What is the relative error in this estimate?

Consider two compartments of linear size s on either side of a cell with diameter a (Fig. 2.2B). If the compartments are aligned with the gradient $\bar{g}$ of a linear concentration profile, then the mean concentrations at each compartment are $\bar{c}_1$ and $\bar{c}_2 = \bar{c}_1 + a\bar{g}$. The mean molecule counts in the two compartments are roughly $\bar{n}_1 = \bar{c}_1 s^3$ and $\bar{n}_2 = \bar{c}_2 s^3$, and the difference is $\Delta \bar{n} = \bar{n}_2 - \bar{n}_1 = a\bar{g}s^3$. The variance in this difference is $\sigma^2_{\Delta n} = \sigma^2_{n_1} + \sigma^2_{n_2} \sim \bar{n}_1^2/(s\bar{c}_1 DT) + \bar{n}_2^2/(s\bar{c}_2 DT)$, where the first step assumes the two compartments are independent, and the second step uses Eq. 2.1 for the variance in each compartment's measurement. For shallow gradients, where the limits on sensing are generally probed, we have $a\bar{g} \ll \bar{c}_1$, and therefore we may assume $\bar{c}_1 \approx \bar{c}_2 \approx \bar{c}$, where $\bar{c}$ is the mean concentration at the center of the cell. Thus $\sigma^2_{\Delta n} \sim 2(\bar{c}s^3)^2/(s\bar{c}DT)$, and the relative error in the cell's estimate of the gradient is then

$$\frac{\sigma_g}{\bar{g}} = \frac{\sigma_{\Delta n}}{\Delta \bar{n}} \sim \sqrt{\frac{\bar{c}}{s(a\bar{g})^2 DT}}, \tag{1.2}$$

where the factor of 2 is neglected in this simple scaling estimate. As in Eq. 2.1, we see that the relative error decreases with s, since the molecule counts in each compartment are larger, and also with D and T, since more independent measurements can

be made. Additionally, the relative error decreases with $a\bar{g}$, since the concentrations measured by the two compartments are more different from each other. However, we see that unlike in Eq. 2.1, the relative error increases with the background concentration $\bar{c}$. The reason is that the cell is not measuring a concentration, but rather a *difference* in concentrations, and it is more difficult to measure a small difference on a larger background than on a smaller background [6]. Eq. 3.1 has been derived more rigorously [32], and the problem has been extended to describe rings of receptors [32] or detectors distributed over the surface of a circle [33] or a sphere [34]. In all cases a term of the form in Eq. 3.1 emerges as the fundamental limit, with the lengthscale s dictated by the particular sensory mechanism and geometry. It is clear that the optimal mechanism would result in an effective compartment size that is roughly half of the cell volume, in which case $s \sim a$.

Do cells reach this limit on gradient sensing? This question has been directly addressed for the amoeba *Dictyostelium discoideum*. Experiments [35] have shown that *Dictyostelium* cells exhibit biased movement when exposed to gradients of cyclic adenosine monophosphate as small as $\bar{g} = 10$ nM/mm, on top of a background concentration of $\bar{c} = 7$ nM. Bias is typically quantified in terms of the chemotactic index (CI), which is the cosine of the angle between the gradient direction and the direction of a cell's actual motion. By relating the error in gradient sensing (a term of the form in Eq. 3.1 with $s = a$) to the error in this angle, Endres and Wingreen [34] obtained an expression for the optimal CI, which they then fit to the experimental data with one free parameter, the integration time T. The inferred value of $T = 3.2$ s serves as the physical lower bound on the response time required to perform chemotaxis. Actual response times of *Dictyostelium* cells, as measured by the time from the addition of a chemoattractant to the peak activity of an observable signaling pathway associated with cell motility [36, 37], are about $5-10$ s. Taken together, these results imply that *Dictyostelium* operates remarkably close to the physical limit to sensory precision set by the physics of molecule counting.

1.1.3 Relative changes vs. absolute molecule numbers

The precision of gradient sensing is often reported in terms of percent concentration change across a cell body. For example, both amoeba [35] and tumor cells [20] are sensitive to a roughly 1% change in concentration across the cell body. However, this method of reporting sensitivity may be misleading. Experiments imply very different sensory thresholds for these cells in terms of absolute molecule numbers, as we will now see.

The key is that it takes two numbers to specify the conditions for gradient sensing: the mean gradient $\bar{g}$ and the mean background concentration $\bar{c}$. For the amoeba *Dictyostelium*, these numbers are $\bar{g} = 10$ nM/mm and $\bar{c} = 7$ nM at the sensory threshold [35]. Given a typical cell size of $a = 10$ μm, these values imply a mean percent concentration change of $\bar{p} = a\bar{g}/\bar{c} = 1.4\%$ (Table 2.1). However, we may also compute from these values the mean molecule number difference $\Delta\bar{n} = a\bar{g}s^3$ from one side of the cell to the other, within the effective compartments of size s. Taking $s \sim a$ gives the maximal molecule number difference of $\Delta\bar{n} = a^4\bar{g} = 60$ for *Dictyostelium* (Table 2.1). Together $\bar{p}$ and $\Delta\bar{n}$ specify the sensing conditions as completely as $\bar{g}$ and $\bar{c}$ do.

Experiments [20] have shown that breast cancer tumor cells exhibit a chemotactic response in a gradient $\bar{g} = 550$ nM/mm of the cytokine CCL21, on top of a background concentration of $\bar{c} = 1100$ nM. Given a typical cell size of $a = 20$ μm, this corresponds to a percent difference of $\bar{p} = a\bar{g}/\bar{c} = 1\%$, similar to *Dictyostelium*. Yet, this also corresponds to a maximal molecule number difference of $\Delta\bar{n} = a^4\bar{g} = 53,000$, which is much higher than that of *Dictyostelium* (Table 2.1). Even though the sensitivities are similar in terms of percent change, they are very different in terms of absolute molecule number.

Lower molecule numbers correspond to higher relative error. We can see this explicitly by writing Eq. 3.1 in terms of the percent change $\bar{p} = a\bar{g}/\bar{c}$. Defining $\epsilon = \sigma_g/\bar{g}$ and taking $s \sim a$, we have $\epsilon \sim 1/\sqrt{\bar{p}^2 a\bar{c}DT}$. Accounting for the fact

that tumor cells (TC) have roughly twice the diameter as *Dictyostelium* cells (DC), this expression implies that the sensitivities of the two cell types over the same integration time T to chemoattractants with the same diffusion constant D satisfy $\epsilon_{\text{DC}}/\epsilon_{\text{TC}} = \sqrt{2\bar{c}_{\text{TC}}/\bar{c}_{\text{DC}}} \approx 18$. We see that because the *Dictyostelium* experiments were performed at lower background concentration, corresponding to lower absolute molecule numbers, the relative error in gradient sensing is 18 times that of the tumor cells, despite the fact that both cell types are responsive to 1% concentration gradients. Therefore, it is important to take note of the background concentration when studying the precision of gradient sensing. These data imply that *Dictyostelium* cells can sense noisier gradients than tumor cells. However, *Dictyostelium* cells have been studied more extensively than tumor cells as exemplars of gradient detection. It remains an interesting open question what is the minimum gradient that tumor cells can detect, not only in terms of percent concentration change, but also in terms of absolute molecule number differences.

1.1.4 Multicellular gradient sensing

In many cancer types, tumor cells invade the surrounding tissue in a collective manner [13, 19]. Cell collectives can sense shallower gradients than single cells, both in terms of percent concentration changes and absolute molecule numbers (Table 2.1). Indeed, groups of neurons respond to gradients equivalent to a difference of less than one molecule across an individual neuron's growth cone [7]. This raises the possibility that during the invasion process tumor cell collectives benefit from higher sensory precision than single tumor cells.

We can understand immediately from Eq. 3.1 why a multicellular collective would have lower sensory error than a single cell: a collective is larger than a single cell. Therefore, the collective covers a larger portion of the concentration profile, which leads to a larger difference between the concentration measurements on either end, and a lower relative error. In terms of Eq. 3.1, if we consider that cells on the ends

	Single Cell		Multicellular	
	Dictyostelium (Amoeba) [35]	Breast Cancer [20]	Neurons [7]	Mammary Epithelia [6]
Cell Length Scale, a	10 μm	20 μm	10 μm	10 μm
Background Concentration, $\bar{c}$	7 nM	1100 nM	1 nM	2.5 nM
Concentration Gradient, $\bar{g}$	10 nM/mm	550 nM/mm	0.1 nM/mm	0.5 nM/mm
Percent Concentration Difference, $\bar{p} = \bar{g}a/\bar{c}$	1.4%	1.0%	0.1%	0.2%
Molecule Number Difference, $\Delta\bar{n} = \bar{g}a^4$	60	53,000	0.6	3

Table 1.1.
Gradient sensory thresholds for single cells and multicellular collectives. Note that experiments can provide equal percent concentration differences but unequal molecule number differences across a cell body, as seen for amoeba and breast cancer cells. We see that multicellular groups can detect smaller gradients than single cells by all measures.

act as the molecule-counting compartments, $s \to a$, and that the entire collective acts as the detector, $a \to Na$, where N is the number of cells in the gradient direction, then we have [8]

$$\frac{\sigma_g}{\bar{g}} \sim \sqrt{\frac{\bar{c}}{a(Na\bar{g})^2 DT}}. \tag{1.3}$$

We see that, as expected, the relative error goes down with the size Na of the multicellular collective.

However, there is a crucial point that is overlooked in formulating Eq. 3.2: the larger the group of cells, the more difficult it is for cells on either end to communicate

the measurement information. This fact is not accounted for in Eq. 3.2. Instead, we see that the relative error decreases with the separation Na between the end cells without bound, which is unrealistic. For a single cell it may be a reasonable approximation to assume that compartments quickly and reliably communicate information across the cell body, but for a multicellular collective, the communication process cannot be overlooked. Importantly, the communication mechanism of multicellular collectives may introduce additional noise into the gradient sensing process. Therefore, it is imperative when considering collective sensing to properly account for the effects of communication.

Recently, the physical limits to collective gradient sensing including communication effects were derived [6, 8]. Communication was modeled using a multicellular version of the local excitation–global inhibition (LEGI) paradigm [9], in which each cell produces a "local" and a "global" molecular species in response to the chemoattractant, and the global species is exchanged between cells to provide the communication (Fig. 2.2C). The difference between local and global molecule numbers in a given cell provides the readout. A positive difference informs the cell that its detected chemoattractant concentration is above the spatial average among its neighbors, and therefore that the cell is located up the gradient, not down. In this model, the relative error of gradient sensing was shown [8] to be limited from below by

$$\frac{\sigma_g}{\bar{g}} \sim \sqrt{\frac{\bar{c}}{a(n_0 a \bar{g})^2 DT}}, \tag{1.4}$$

where n_0^2 is the ratio of the cell-to-cell exchange rate to the degradation rate of the global species. Comparing Eq. 3.2 to Eq. 3.4, we see that without communication the error decreases indefinitely with the size Na of the collective, whereas with communication the error is bounded by that of a collective with effective size $n_0 a$. Evidently, communication defines an effective number of cells n_0 over which information can be reliably conveyed, and a collective that grows beyond this size no longer improves its sensory precision.

These theoretical predictions were tested experimentally in collectives of epithelial cells [6]. Mouse mammary epithelial cells were grown in organotypic culture and sub-

jected to very shallow gradients of epidermal growth factor (Table 2.1). It was shown that while single cells did not respond to these gradients, the multicellular collectives did: they exhibited a biased cell-branching response. Importantly, the response of large collectives was no more biased than the response of small collectives, supporting the theory with communication (Eq. 3.4) over the theory without communication (Eq. 3.2). The effective detector size was inferred to be $n_0 \approx 3.5$ cells, which is consistent with the size of these collectives in their natural context (the "end buds" of growing mammary ducts) [38]. Interestingly, when the gap junctions between cells, which mediate the molecular communication, were blocked with each of several drugs, the biased responses were abolished [6], demonstrating that the collective response was critically dependent on the cell-to-cell communication. Taken together, these results indicate that cell-to-cell communication is a necessary but imperfect enabler of collective gradient sensing. The results also speak to the power of simple physical theory to quantitatively explain collective cellular capabilities. Since epithelial cancers are known to invade collectively [13], it remains an important open question whether this theory also describes the sensory behavior of tumor cell collectives.

1.2   Physical models of collective migration

Metastatic invasion is a process of cell migration. Collective invasion, in turn, is a process of collective migration. Therefore, it is important to understand not only the collective sensing capabilities of tumor cells, but also the properties of their collective migration—and ideally the relation between the two. From a physical modeling perspective, describing collective cell dynamics is an interesting problem, because often rich and unexpected behavior can emerge from a few simple interaction rules between cells. Even in the absence of sensing, simple models have successfully explained observed collective behaviors such as cell streaming, cell sorting, cell sheet migration, wound healing, and cell aggregation [15–18]. Here we focus on the collective dynamics that emerge when sensing plays a key role. In this case, a sensory cue results in

polarization of a cell or cell collective via one of a variety of mechanisms [31], and the dynamics are directed, i.e. migratory.

1.2.1 Mechanisms of collective migration

Broadly speaking, the mechanisms of collective migration can be divided into three categories. First, cells may exhibit individual sensing and individual migration (Fig. 2.3A). Here, each cell can perform gradient sensing and migration individually, although the precision may be low. When many such cells are placed in a group, the group migration can be enhanced and focused by local interactions between the cells. Even if each individual cell has low sensory and migratory precision, the precision of the group as a whole is high due to the interactions. This mechanism is often termed "many wrongs," and it is successful at explaining how group migratory behavior emerges from individual agents that act independently [39]. For example, a recent study demonstrated that single-cell chemotaxis can be improved through collisions between cells which align cell polarization in the gradient direction [40]. Collisions act to average over the errors in individual cells' noisy measurements, thereby decoupling group behavior from single-cell properties.

Second, cells may exhibit individual sensing but collective migration (Fig. 2.3B). In this mechanism, each individual cell senses its own local environment, and tight mechanical interactions result in the emergent directed motion of the entire group. This mechanism is applicable to the collective migration of connected clusters of cells. For example, a model of this type was recently developed by Camley et al. to describe behavior seen in clusters of neural crest cells and other cell types [41]. In this model, cells are tightly connected but are polarized away from neighboring cells due to contact inhibition of locomotion (CIL), the physical phenomenon of cells ceasing motion in the direction of cell-cell contact [42]. Individual cells sense a local chemoattractant concentration and attempt to migrate away from the group with a strength proportional to this concentration. However, the mechanical coupling
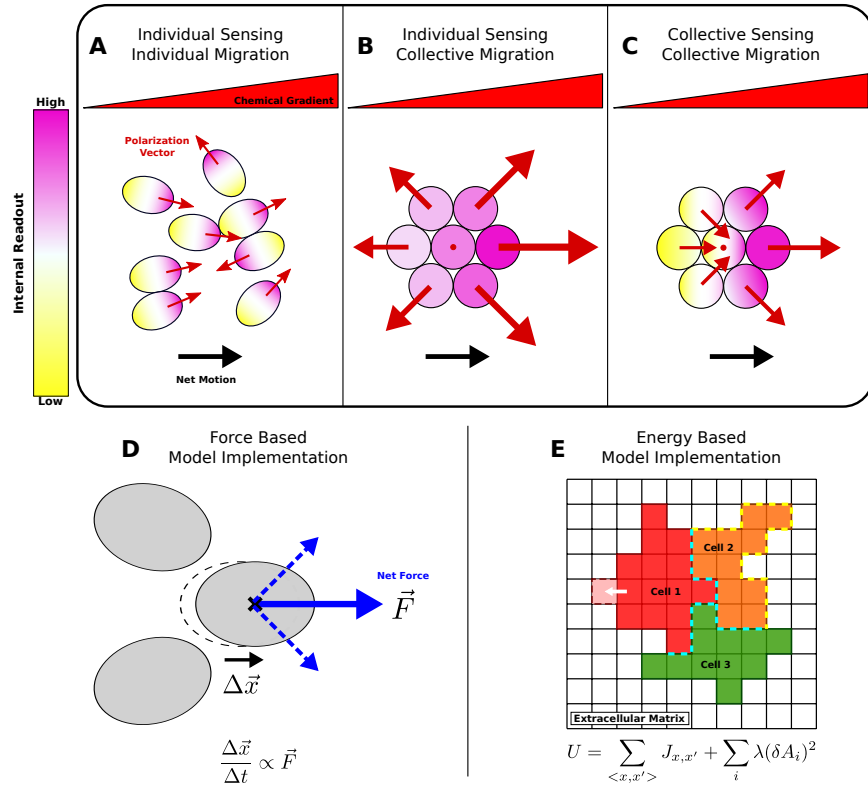
Fig. 1.3. Mechanisms of collective migration: (A) individual sensing and migration (the "many wrongs" mechanism), (B) individual sensing but collective migration (emergent chemotaxis), and (C) collective sensing and migration. Implementations of collective migration: (D) in force-based models, dynamics evolve from stochastic forces acting on each cell; (E) in energy-based models, dynamics evolve via energy minimization with thermal noise. E shows the cellular Potts model framework, in which cells are collections of lattice sites, and cell-cell (dashed blue) and cell-environment (dashed yellow) contacts contribute to the energy of the system.

keeps them together. In the presence of a concentration gradient, the imbalance in their migration strengths results in net directed motion (Fig. 2.3B). Notably, this mechanism results in directed motion of a cluster even though individual cells cannot execute directed motion alone, since without other cells, there is no CIL to bias the motion.

Third, cells may exhibit collective sensing and collective migration (Fig. 2.3C). As discussed above, multicellular groups exploit cell-to-cell communication to sense gradients collectively, thereby enhancing the precision of sensing. A feature of this collective sensing, e.g. via the multicellular LEGI mechanism discussed above [6, 8], is that each cell has information on the extent to which it is up or down the gradient. Through CIL or other contact-mediated interactions, this information can translate directly into cell polarity, leading to more coherent collective migration than in the previous mechanism (Fig. 2.3C vs. B). In fact, the multicellular LEGI model was used by Camley et al. [41] to explore a model of this type. Adding collective sensing to their model of CIL-dependent migration gave the advantage that the repulsive tension on a cell cluster was adaptive and therefore remained constant as the cluster migrated to regions of higher chemical concentration.

1.2.2 Model implementations

To study the above mechanisms quantitatively and compare predictions with experiments, one must turn to mathematical and computational modeling. Models of cell dynamics range from continuum or semi-continuum descriptions, which describe groups of cells as continuous tissues, to individual-based models, which describe cells as individual interacting entities [43]. Physics-driven individual-based models generally fall into two categories: force-based models and energy-based models.

Force-based models (Fig. 2.3D) typically represent cells as centers of mass or as collections of vertices. Cell dynamics evolve from forces acting on individual cells, which can be stochastic, and arise from internal features such as cell polarity, and external features such as mechanical interactions with other cells [43]. Force-based models are able to reproduce multicellular behavior such as chemotaxis, wound healing, and cell aggregation [17, 18, 41]. Parameters are often directly relatable to experimental measurements, and the simplest models are often amenable to exact mathematical analysis [41].

Energy-based models (Fig. 2.3E) allow cell dynamics to emerge from the minimization of a potential energy with thermal noise (the so-called Monte Carlo scheme). A widely used example is the cellular Potts model (CPM) [44, 45], in which cells are represented as collections of co-aligned "spins" on a lattice (Fig. 2.3E). Cells remain contiguous because it is energetically favorable for neighboring spins to be co-aligned. Biophysical features such as cell shape, cell-cell adhesion, and cell protrusions into the environment are modeled by introducing corresponding terms into the global potential energy. The CPM has been used to describe cell sorting, streaming, and chemotaxis [46] and has successfully reproduced experimental observations of epithelial streaming, cell sorting, and collective migration [15, 16, 46]. In energy-based models, the parameters are less directly relatable to experiments; rather, their values can often be set by calibrating emergent features, such as cell diffusion coefficients or average speeds, with experimental measurements [16].

Although the physical limits to multicellular sensing are becoming better understood, the physical limits constraining multicellular migration are less clear. This remains an interesting open question, and answering it will require integrating the theories of sensing and communication with the models of collective migration described herein. For tumor cells in particular, an integrated physical theory of sensing and migration would prove immensely useful for identifying the key determinants of invasive capabilities. Identifying these determinants would help pinpoint the ways that these capabilities could be disrupted, using drugs and other therapies, as described next.

1.3 Drug sensitivity and implications for therapy

We have seen that cells, including tumor cells, are remarkably precise sensors of molecules in their environment. This raises the question of how sensitive tumor cells are to drug molecules in their environment. What is the minimum drug concentration

Outcome	Drug Concentration	Molecules per Cell
Physical change [47]	1 nM	5,000
Cell death [48]	10^4 nM	5×10^7
Cell death, nanoparticle delivery [49]	100 nM	500,000
Communication blockage [6]	50 nM	30,000

Table 1.2.

Drug sensitivity thresholds. Molecules per cell volume are calculated assuming a cubic cell of length $a = 20$ μm for tumor cells (rows 1-3) and $a = 10$ μm for epithelial cells (row 4).

required not just for precise detection by a cell, but for causing a phenotypic change, such as cell death?

Experiments have shown that cancer cells are sensitive to very small drug concentrations. For example, lung carcinoma cells were exposed *in vitro* to various concentrations of the anti-cancer drug paclitaxel, also known as taxol, which acts to block mitosis in order to achieve cell death by disrupting microtubule regulation [47]. Pacltaxel concentrations as low as 1 nM were shown to affect microtubule dynamics of the cells. This concentration is commensurate with the smallest background concentrations in which cells can perform gradient sensing (Table 2.1). Assuming a cell length of 20 μm, this concentration corresponds to only a few thousand drug molecules in the volume of a cell (Table 2.2). Evidently lung cancer cells are affected by drug concentrations that are near the fundamental limits of what can be sensed.

Although cancer cells may be very sensitive to small drug concentrations, that does not translate to successful treatment. In order to achieve cell death, much larger drug concentrations are required. In the same study on lung carcinoma cells, cell death was observed for drug concentrations on the order of 10 nM and greater. More typical drug concentrations required for cell death are on the order of micromolars. For instance, it has been shown *in vitro* that anticancer drug concentrations on the

order of 10 μM are required to kill at least 90% of tumor cells [48]. With a cell length of 20 μm, 10 μM corresponds to tens of millions of drug molecules in the volume of a cell, four orders of magnitude greater than drug concentrations required to affect cell functionality (Table 2.2). In order to effectively kill a solid tumor, very high drug doses are required.

Complicating matters is the fact that the tumor and its surrounding microenvironment comprise a complex and heterogeneous system. Although most cells in the human body are naturally within a few cell lengths of a blood vessel, due to high proliferation tumor cells may be upwards of tens of cell lengths away from a vessel [50]. This makes it difficult for drugs to reach the tumor. Moreover, the high density of many solid tumors causes gradients of drug concentration to form as a function of tumor radius [51]. This results in a reduced drug concentration at the center of the tumor and makes innermost tumor cells the most difficult to kill. A promising way to overcome this difficulty is through the use of nanoparticle drug delivery systems, which increase both the specificity and penetration of drugs to the tumor. Nanoparticle delivery has been shown [49] to achieve cell death with concentrations as low as 100 nM. Although this concentration is lower than for delivery without nanoparticles, it is still two orders of magnitude higher than the minimum concentration that causes physical changes in the cell (Table 2.2). Even with targeted delivery, achieving drug-induced tumor cell death remains a challenging task.

Given this challenge, we may hope to draw upon the physical insights reviewed herein to devise therapeutic strategies that are alternative or complementary to comprehensive cell death. Specifically, we imagine focusing on the metastatic invasion phase, and targeting the functions of invading tumor cells, including communication and migration, in addition to targeting cells' overall viability, to produce better treatment (Fig. 2.1C). Communication is a particularly promising candidate, since it has recently been shown that cell-to-cell communication makes cancer cells more resistant to therapy and helps sustain tumor growth [12]. Indeed, the exchange of extracellular vesicles, which is a form of communication observed between tumor cells and stromal

cells, has been linked to immune suppression, tumor development, angiogensis, and metastasis [14]. This suggests that disrupting cell-to-cell communication could be an effective strategy for stopping tumor progression or curbing metastatic invasion. Disrupting communication may not require concentrations as large as those necessary for cell death, which are difficult to maintain *in vivo* across the whole tumor. For example, as little as 50 nM of the gap-junction-blocking drug Endothelin-1 is sufficient to remove collective responses in epithelial cells [6]. This concentration is several orders of magnitude smaller than that required for comprehensive cell death, and it is on the order of concentrations that are effective with targeted nanoparticle delivery (Table 2.2). Therefore, it is tempting to suggest that managing metastatic invasion by blocking communication or other cell functions is a more accessible therapeutic strategy than eradicating a tumor outright.

1.4   Outlook

In this review, we have taken a quantitative look at metastatic invasion as a sensing-and-migration process, which has allowed us to compare metastatic cells to other cell types in terms of their physical capabilities. We have seen that tumor cells can sense very shallow chemoattractant gradients, which may help guide metastatic invasion, but it remains unclear whether tumor cells operate near fundamental sensing limits, as bacteria and amoeba do. Recognizing that metastatic invasion can be collective, we have reviewed recent results on the physical limits to collective sensing, and we have identified the overarching mechanisms of collective migration. A key insight that emerges is that collective capabilities rely critically on cell-to-cell communication. This insight opens up alternative strategies for therapy that target specific cell capabilities such as communication, in addition to strategies that aim for comprehensive cell death.

Moving forward, it will be important to identify whether the physical theory of sensing reviewed herein can be applied in a predictive manner to tumor cells, and

whether gradient sensing plays a dominant role during metastatic invasion. More generally, it will be necessary to integrate the theory of sensing with models of collective migration to predict quantitatively what groups of migratory cells can and cannot do. Finally, controlled experiments with metastatic cells are required to validate these predictions, and to assess the viability of alternative therapies that target specific cell functions in order to combat metastatic invasion. Our hope is that the integrated, physics-based perspective presented herein will help generate innovative solutions to the pervasive problem of metastatic disease.

2. DYNAMICS OF COLLECTIVE CHEMOTAXIS

Cells can migrate in response to a chemoattractant and can detect extraordinarily small changes in chemical concentrations. The limits to cell sensory precision have been a topic of research in biology and biophysics for many years. *Escheria coli* bacterial chemotaxis operates very near the physical limits of their sensory machinery, and *Dictyostelium discoideum* amoebae are sensitive to differences in chemical concentrations on the order of ten molecules across the cell [1, 2]. Recent studies on individual breast cancer cells showed that they are sensitive to 1% differences in concentration across the cell length [20]. Limits to cell sensory precision were first derived by Berg and Purcell almost 40 years ago [2] and have been revisited to account for binding kinetics, spatiotemporal correlations and spatial confinement [3–5]. However, in nature cells are rarely found alone, and the interactions between nearby cells may alter cells' sensory capabilities.

In many biological contexts cells act in close proximity to one another which can have significant effects on collective behavior. Clusters of mammary epithelial cells, lymphocytes and neural crest cells can detect chemical gradients that single cells cannot [6, 52, 53], and cultures of neurons have been shown to be sensitive to single molecule differences across an individual neuron's axonal growth cone [7]. In many types of cancer, tumor cell invasion is collective, involving coherent grouped motion guided by chemical cues [13, 19, 26, 29]. It is clear from these examples that cells acting collectively can improve upon their individual sensory precision. Similar to the limits set by Berg and Purcell, the physical limits to collective gradient sensing have been recently derived [6, 8] by using a multicellular version of the local excitation-global inhibition (LEGI) communication model [9], one of the simplest adaptive mechanisms of gradient sensing. With these studies the physical limits of cell sensing have been extended from single cells to multicellular collectives.

In parallel to research on cell sensory precision, studies on collective cell migration have also advanced. Biological processes such as development, cellular migration, pathogenic response, and cancer progression all involve many cells acting in a coordinated way [10–14, 54, 55]. Simple mechanical models successfully explain observed collective behaviors such as cell streaming, cell sorting, cell sheet migration, wound healing, and cell aggregation [15–18]. These models accurately model collective cell migration but fail to explicitly include the affects of multicellular sensing in driving the mechanics at play. Cells are often capable of intercellular communication, so understanding how communicated information is translated into mechanical action is of prime interest.

How the phenomena of collective sensing and multicellular migration are connected remains an open question [56–58]. Recent studies by Camley et al. [41] and Malet-Engra et al. [52] have started to address this need for modeling collective sensing and migration. In the study of Camley et al. individual cell measurements act to polarize cells in a cluster outwards causing tension, and when intercellular communication is added the tension on the cluster adapts to the chemical concentration. Both studies do not take into account the inherent stochasticity of cell sensing and intercellular communication. However, individual cell measurements of the environment are error-prone while propagation of single cell measurements also adds noise to the system. These studies also treat cells or clusters as perfect circles, neglecting natural geometric fluctuations in the size and shapes of cells that occur during migration.

Here we focus our attention on stochastic processes governing collective gradient sensing and cell motility. First, the limits to collective gradient sensing are briefly reviewed and our implementation of multicellular LEGI described. Information gained from collective sensing then must be used to direct cell motion. We develop a model which takes into account the fluctuating shape of cells while coupling cell motility to noisy collective gradient sensing. We model intercellular communication via the direct exchange of messenger molecules between cells. Candidate mediators of such intercellular communication have been recently identified in *Drosophila* devel-
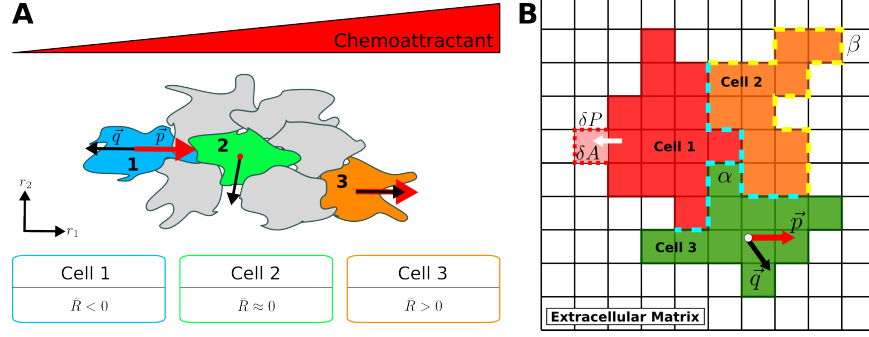
Fig. 2.1. Model implementation. (A) Cell polarization is biased by multicellular sensing. On average, the cells on the left and right edges will measure negative and positive values of R, respectively. This causes the left-edge (Cell 1) and right-edge (Cell 3) cells to polarize in the direction of the gradient, while cells in the middle (Cell 2) are on average not polarized since $\bar{R} \approx 0$. Polarization vectors $\vec{p}$ are red, repulsion vectors $\vec{q}$ are black. (B) Simulations are implemented using the Cellular Potts Model (CPM). Cells comprise of simply connected lattice points. There are adhesion energies associated with different types of contact: cell-cell, α (blue-dashed line), and cell-ECM, β (yellow-dashed line). Cell motility is modeled by the addition/removal of lattice points (pink). Each cell has a center-of-mass (white dot), a polarization vector, $\vec{p}$ (red) and a repulsion vector, $\vec{q}$ (black).

opment [59], and other studies suggest intercellular communication's involvement in organoid branching, angiogenesis, and cancer [6, 60–62]. We study cluster migration in shallow gradients where the change in concentration across a cell width is very small relative to the background concentration. This regime is of prime interest since experiments show that collectives can respond to these shallow gradients whereas single cells cannot [6, 7, 52]. By explicitly modeling the stochastic processes of sensing and migration this model places constraints on the collective behavior of cells and predicts an optimal cluster size for fastest chemotaxis. We conclude by discussing our model's implications for cell migration experiments.

2.1 MODEL

Communication between cells and collective sensing can improve upon an individual cell's ability to sense the environment [6], and in turn this information may be used to direct cell motion. To describe collective sensing, we will use the well-established local excitation–global inhibition (LEGI) mechanism [8,9].

2.1.1 Limits to Multicellular Sensing

Individual cells measure spatial gradients by comparing concentration measurements c made by receptors or groups of receptors on the cell surface [8, 31]. For simplicity, we assume that a cell of size a compares the number of diffusing molecules within two different regions of size b which run parallel to the chemical gradient $\bar{g}$. The relative error in each compartment's measurement is $(\sigma_c/\bar{c})^2 \sim 1/(b\bar{c}DT)$ [2], where D is the diffusion coefficient, and T is the measurement integration time. Assuming that the measurements made in each compartment are independent, then the difference in counts is proportional to the gradient $\Delta\bar{n} = \bar{n}_2 - \bar{n}_1 \sim ab^3\bar{g}$. In the limit that the gradient is very small relative to the background concentration $a\bar{g} \ll \bar{c}$, the relative error in gradient sensing simplifies to

$$\frac{\sigma_g}{\bar{g}} = \frac{\sigma_{\Delta n}}{\Delta\bar{n}} \sim \sqrt{\frac{\bar{c}}{b(a\bar{g})^2 DT}}. \tag{2.1}$$

Eq. 3.1 has been extensively derived and generalized to systems with different geometries [32–34] and in all such cases a term of the form in Eq. 3.1 appears as the fundamental limit, with the length scale b dictated by the particular sensory mechanism and geometry. In the case of multicellular gradient sensing, we consider the cells on opposite ends of a chain of cells as the two compartments comparing concentration measurements. Then in Eq. 3.1 $b \to a$ and $a \to Na$ where N is the number of cells in the chain. The relative error for the multicellular cluster becomes [8]

$$\frac{\sigma_g}{\bar{g}} \sim \sqrt{\frac{\bar{c}}{a(Na\bar{g})^2 DT}}. \tag{2.2}$$

There is a crucial effect that is neglected in formulating Eq. 3.2 which is the mechanism by which the cells communicate their measurements across the collective. Communication will introduce additional noise to the gradient sensing process thereby altering the expression for the relative error. In the case of a single cell it is reasonable to assume that measurements from different compartments can be reliably transmitted, but with the increased size of the multicellular cluster we cannot make the same assumption. Using the multicellular LEGI paradigm [9] to model intercellular communication, the physical limits to communication-aided collective gradient sensing have been derived [6,8], which we expand upon below.

2.1.2 Multicellular LEGI Model

In the LEGI model cells produce two chemical species, a "local" species X, and a "global" species Y, in response to the chemoattractant S. The local species X remains within an individual cell and represents that cell's measurement of its local chemical concentration. This species can be a molecule produced or activated in response to attractant-bound receptors, or the bound receptors themselves. The global species Y can diffuse at the rate γ between neighboring cells and therefore represents the average X population among neighboring cells. Y molecules may only be exchanged when two or more cells are in direct contact with one another. Recent experiments in epithelial cells identified this global species as either calcium or a small molecule involved in calcium signaling (such as IP3), and identified the intercell diffusion mechanism as mediated by gap junctions [6]. Finally, X activates a downstream reporter molecule R, while Y inhibits R.

Let x_k, y_k, and R_k represent the molecule populations in X, Y, and R in the kth cell. The chemical reactions in cell k are

$$
\begin{aligned}
s_k &\xrightarrow{\kappa} s_k + x_k \qquad x_k \xrightarrow{\mu} \emptyset \\
s_k &\xrightarrow{\kappa} s_k + y_k \qquad y_k \xrightarrow{\mu} \emptyset \qquad y_k \underset{\gamma_{j,k}}{\overset{\gamma_{k,j}}{\rightleftharpoons}} y_j.
\end{aligned}
\tag{2.3}
$$
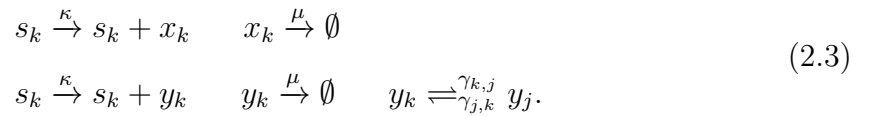
The production and degradation rates for X and Y are κ and μ, respectively. The global reporter molecule exchange rate γ is dependent on the length of the interface $\mathcal{C}$ made between adjacent cells, and on the exchange rate per unit contact-length Γ,

$$\gamma_{j,k} = \int_{\mathcal{C}} \Gamma dl.$$

In the limit of strong communication ($\gamma \gg \mu$) and many cells, the relative error of gradient sensing is limited from below by [8]

$$\frac{\sigma_g}{\bar{g}} \sim \sqrt{\frac{\bar{c}}{a(n_0 a \bar{g})^2 DT}}, \tag{2.4}$$

where n_0 sets an effective number of cells over which information can be reliably conveyed. In our model communication between cells improves with increased diffusion of Y molecules and so $n_0^2 \propto \gamma/\mu$ [6, 8]. As collectives grow larger than n_0 cells the relative error ceases to improve, saturating to the limit set by Eq. 3.4; unlike Eq. 3.2 where the effects of communication are ignored and the relative error decreases without bound.

In the limit of shallow gradients, which are of primary interest in studying collective sensing, R effectively reports the difference in X and Y molecule populations [6] and so we will model the downstream readout as $R_k = x_k - y_k$. A negative (positive) difference indicates that the cell is below (above) the average measured concentration relative to nearby cells as shown by the reported average R values for each cell in Fig. 3.1A.

The chemical concentration is modeled as a space-dependent field $E(r_1, r_2)$, and in this case has a constant gradient in the r_1-direction,

$$E(r_1, r_2) = \bar{g} r_1 + \bar{c}.$$

The average signal in the kth cell's local environment is $\bar{s}_k = \int_{A_k} dr_1 dr_2 \, E(r_1, r_2)$ where A_k is the area of the kth cell. Since diffusion is a Poisson process the variance in the measured signal s_k is equal to the mean, $\sigma_{s_k}^2 = \bar{s}_k$. At each time step we sample s_k for each cell from a Gaussian distribution with mean and variance $\bar{s}_k$, which corresponds

to instantaneous sensory readout [6]. The dynamics of the local reporter satisfy the stochastic differential equation

$$\dot{x}_k = \kappa s_k - \mu x_k + \eta_{x_k}. \tag{2.5}$$

The first term in Eq. 3.5 is due to the production of X molecules due to the signal S, the second term represents molecule degradation, and the third term η_{x_k} accounts for the noise inherent to these reactions. The noise term is equal to $\eta_{x_k} = \sqrt{\kappa \bar{s}_k} \xi_{1,k} - \sqrt{\mu \bar{x}_k} \xi_{2,k}$ since both production and degradation are stochastic processes [63]. In Eq. 3.5 and subsequent stochastic equations $\xi_{i,k}$ and $\chi_{j,k}$ are unit Gaussian random variables representing the noise in molecule populations. For the local reporter, the steady-state solution is simply

$$x_k^{ss} = (\kappa/\mu)\, s_k + (1/\mu)\, \eta_{x_k}. \tag{2.6}$$

The dynamics of the global species can be modeled in similar fashion,

$$\dot{y}_k = \kappa s_k - \mu y_k - y_k \sum_{\langle j,k \rangle} \gamma_{j,k} + \sum_{\langle j,k \rangle} y_j\, \gamma_{j,k} + \eta_{y_k}. \tag{2.7}$$

The first summation term in Eq. 3.7 accounts for the loss of y_k due to the diffusion out to neighboring cells, and similarly the second summation term accounts for the increase in y_k due to diffusion into cell k from its neighbors. The notation $\langle j, k \rangle$ represents the set of all nearest neighbor pairs. The noise term η_{y_k} in the molecule dynamics depends on the production, degradation and diffusion of Y molecules. In steady-state we can express the noise as

$$\eta_{y_k} = \sqrt{\kappa \bar{s}_k} \xi_4 - \sqrt{\mu \bar{y}_k} \xi_5 + \sum_{j=1}^{N} \left[\chi_{j,k} \sqrt{\gamma_{j,k}} \left(\sqrt{\bar{y}_j} - \sqrt{\bar{y}_k} \right) \right].$$

Similarly to η_{x_k}, the noise in y_k also depends on production and degradation while an extra term is required to account for the noise in Y molecule exchange. Eq. 3.7 can be simplified by noting that exchange rates between cells are symmetric $\gamma_{j,k} = \gamma_{k,j}$, $\gamma_{i,i} = 0$, and by defining the sum of all the exchange rates between cell k and all other

cells as $G_k = \sum_{j=1}^{N} \gamma_{j,k}$. The steady-state solution for the global reporter is more involved than the local reporter, and can be written as a matrix equation

$$M\vec{y}^{ss} = \kappa\vec{s} + \vec{\eta}_y, \tag{2.8}$$

where M is a square, symmetric matrix that governs the degradation and exchange of Y molecules in all cells,

$$M = \begin{bmatrix} \mu + G_1 & -\gamma_{1,2} & \cdots & -\gamma_{1,N} \\ -\gamma_{2,1} & \mu + G_2 & \cdots & -\gamma_{2,N} \\ \vdots & \vdots & \ddots & \vdots \\ -\gamma_{N,1} & -\gamma_{N,2} & \cdots & \mu + G_N \end{bmatrix}. \tag{2.9}$$

Parameter	Value	Notes
Concentration $\bar{c}$	10nM	Assumes $\bar{c} \gg a\bar{g}$ for shallow gradients [6, 52]
Gradient $\bar{g}$	0.04nM/μm	
LEGI Molecule Production Rate κ	19.72min^{-1}	Assumes $\{\kappa, \mu\} \gg r$
LEGI Molecule Degradation Rate μ	19.72min^{-1}	i.e. biochemical signaling is faster than motility response
Global Reporter Exchange Rate Γ	80(μm min)$^{-1}$	Varied in Fig. 3.3
Polarization Bias Strength ϵ	0.8	Varied in Fig. 3.2
Polarization Decay Rate r	3.94min^{-1}	Sets polarization memory time, as used in [16]
Relaxed Cell Area A_0	315μm^2	Assumes cell radius 10μm [21]
Relaxed Cell Perimeter P_0	3.6$\sqrt{A_0}\mu$m	Assumes circular resting shape
Cell-cell Contact Energy α	1.0	Sets energy scale
Cell-ECM Contact Energy β	3.5	$2\beta > \alpha$ for cell adhesion [44] (Varied in Fig. 3.2)
Area Energy Cost λ_A	1.5	Prevents "stringy" cell-shapes
Area Energy Cost λ_P	0.01	

Table 2.1.
Table of parameter values. Energy costs are in units of $k_B T$, where $k_B T$ is the thermal energy of the CPM Monte Carlo scheme.

2.1.3 Connecting Gradient Sensing to Cell Motility

To describe collective migration, we integrate the output of multicellular LEGI gradient sensing with cell motility. Cells in motion have a distinct front and are polarized along the direction of the front to back. Cells within the cluster have their polarization biased by a combination of the LEGI readout and intercellular repulsion due to contact inhibition of locomotion (CIL). CIL is the phenomenon where cells that come into contact cease to form protrusions in the direction of contact [42]. This is a very simple way for cells to translate the noisy, error-prone gradient measurements into collective cell motility [41, 52, 53].

In order to connect sensing to motility, we couple individual cell polarization $\vec{p}$ to both the LEGI downstream readout R and what we will call the cell's repulsion vector $\vec{q}$. The cell's polarization vector represents the desired direction of motion [31] and modeling collective behavior using cell polarization has been done previously [16, 41]. Information about the cell's surroundings are naturally expressed by the repulsion vector $\vec{q}$ [41]. The repulsion vector is representative of contact inhibition of locomotion (CIL) [42]. CIL demonstrates that cells are aware of their immediate surroundings. The repulsion vector for cell k is a unit vector that points away from all of cell k's neighbors.

$$\vec{q}_k = \left(\frac{1}{\sum_{\langle j,k \rangle} L_{j,k} |\vec{x}_k - \vec{x}_j|} \right) \sum_{\langle j,k \rangle} L_{j,k} \left(\vec{x}_k - \vec{x}_j \right), \qquad (2.10)$$

where $L_{j,k}$ is the contact length made between cell k and its neighboring cell j. In our model cell polarization will change as a function of time depending on a combination of the repulsion vector and the LEGI downstream readout,

$$\frac{d\vec{p}_k}{dt} = r \left[-\vec{p}_k + \epsilon \frac{R_k}{\sigma_R} \vec{q}_k \right]. \qquad (2.11)$$

The first term in Eq. 3.11 models the decay of cell polarization. In the absence of any stimulus an individual cell will undergo a persistent random walk with a timescale $1/r$ [16]. The second term acts to align or anti-align the cells polarization vector with the repulsion vector, with alignment strength ϵ based on the cell's readout R_k.

The magnitude of R_k is normalized by its standard deviation σ_R. The net effect is illustrated in Fig. 3.1A.

In the presence of a gradient, cells on the edge near the lower-end of the chemical concentration will tend to be polarized into the cluster (Cell 1 in Fig. 3.1A), whereas cells on the higher concentration edge tend to be polarized outwards (Cell 3 in Fig. 3.1A). Cells in the center of the cluster (Cell 2 in Fig. 3.1A) are on average unpolarized. The net effect is that the cells on the edges of the cluster will drive motion in the direction of increasing chemical concentration. It is important to note that in this model single cells are unable to chemotax since the multicellular LEGI mechanism requires more than one cell to detect a gradient, and similarly without neighboring cells there is no repulsion vector to bias the cell's polarization.

2.1.4 Computational Implementation

Computational simulations are conducted in order to understand the dynamics that evolve from the model of collective sensing and migration. The source code for the simulations can be found here [64]. The implementation chosen is the Cellular Potts Model (CPM) [44, 45] although other cellular automata models are possible as well [65–67]. The CPM is widely used for simulating cell-centric systems. Despite its relative simplicity, this computational implementation can qualitatively reproduce diverse biological phenomena [46]. The CPM is a very good implementation for simulating systems wherein cell geometry is crucial to the dynamics of the system. Using CPM many studies, some involving cell polarization and mechanical-based coupling, successfully reproduce epithelial cell streaming, cell sorting, chemotaxis and collective migration [15, 16, 43].

In the CPM cells exist on a discrete lattice and are represented as groupings of lattice points. Simply-connected groups of lattice sites x with the same integer values for their *lattice label* $\sigma(x) > 0$ comprise a single cell. The extracellular matrix (ECM) is labeled with the lattice label $\sigma(x) = 0$. Cells have a desired size and perimeter

from which they can fluctuate, and cells adhere to their neighboring environment with an associated adhesion energy. The energy of the whole system is the sum of contributions from adhesion $J_{i,j}$, area-restriction λ_A, and perimeter-restriction λ_P terms,

$$u = \sum_{\langle x,x' \rangle} J_{\sigma(x),\sigma(x')} + \sum_{i=1}^{N} \left(\lambda_A (\delta A_i)^2 + \lambda_P (\delta P_i)^2 \right), \qquad (2.12)$$

$$J_{\sigma(x),\sigma(x')} = \begin{cases} 0 & \sigma(x) = \sigma(x') \text{ (within the same cell)}, \\ \alpha & \sigma(x)\sigma(x') > 0 \text{ (cell-cell contact)}, \\ \beta & \sigma(x)\sigma(x') = 0 \text{ (cell-ECM contact)}. \end{cases} \qquad (2.13)$$

The parameters α and β characterize intercellular adhesiveness, and in order to ensure that it is energetically favorable for cells to remain in contact, we restrict $\beta > 2\alpha$ [16]. β represents the cell-ECM contact energy, a larger value corresponds to an ECM that is more difficult to traverse. Heterogeneities in the microenvironment could be represented by a spatially dependent β; here we take β to be a constant. The area- and perimeter-restriction energy terms prevent cells from growing or shrinking to unphysical sizes as well as branching or stretching into unphysical shapes. Cells fluctuate in shape and size around the desired area A_0 and perimeter P_0 with $\delta A_i \equiv A_i - A_0$ (and similarly for δP_i). The resulting dynamics evolve from the minimization of the system's energy under thermal fluctuations.

Cell dynamics are a consequence of minimizing the energy of the whole system. This is a random process that is sensitive to thermal fluctuations and is modeled using a Monte Carlo process. In a system of n lattice sites, one *Monte Carlo* time step (MC step) is composed of n *elementary* steps. Each elementary step consists of an attempt to copy the lattice label of a randomly chosen lattice site onto that of a randomly chosen neighboring site as illustrated by the pink lattice site in Fig. 3.1B. The new configuration resulting from the copy is accepted with probability P, which

depends on the change in the system's energy accrued in copying over the lattice label,

$$P = \begin{cases} e^{-(\Delta u - w)} & \Delta u - w > 0, \\ 1 & \Delta u - w \leq 0. \end{cases} \tag{2.14}$$

The term Δu is the change in energy of the system due to the proposed lattice label copy. w is the *bias* term which acts to bias cell motion in the direction of polarization. The bias term in the CPM model is required in order for cell clusters to exhibit directed motion [16],

$$w = \sum_{k=\sigma(a),\sigma(b)} \frac{\Delta \vec{x}_{k(a \to b)} \cdot \vec{p}_k}{|\Delta \vec{x}_{k(a \to b)}||\Delta \vec{x}_{k(\Delta t)}|}. \tag{2.15}$$

The summation in Eq. 3.15 is over the cells involved in the elementary time step: a is the lattice site being copied, and b is the lattice site being changed. The change in the cell's center of mass position during the elementary time step is $\Delta \vec{x}_{k(a \to b)}$, whereas $\Delta \vec{x}_{k(\Delta t)}$ is the cell's change in the center of mass during a MC step. The cell polarization vector $\vec{p}_k$ is updated at every MC step in accordance with Eq. 3.11. The dot product acts to bias cell motion since movement that is parallel to the polarization vector will result in a more positive w which in turn results in a higher acceptance probability (Eq. 3.14).

In addition to calculating the energy of the system, at each MC step the X and Y molecule populations in each cell are sampled by solving Eq. 3.6 and 3.8. In doing so our model accounts for fluctuations in molecule numbers, cell shape, and cell-cell contact. With this computational implementation cells on the edges of the cluster are polarized in the direction of increasing chemical concentration, and cells near the center of the cluster have no net polarization, resulting in collective migration in the direction of increasing chemical concentration.

2.2 Results

We simulate clusters of various sizes migrating in response to shallow constant chemical gradients over a fixed distance (Fig. 3.2A, Movie S1). The simulation results
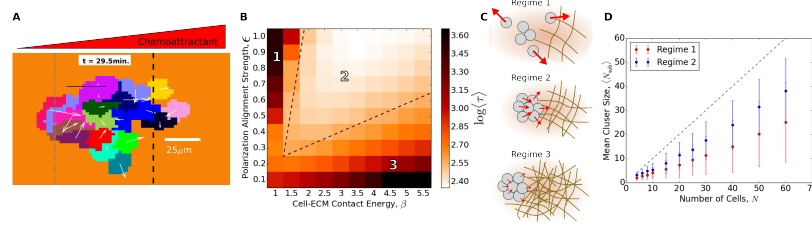
Fig. 2.2. Characterizing the emergent multicellular migration. (A) Snapshot from simulation. Individual cells are distinguished by color and white arrows represent their polarization vectors. The cluster centroid is initially located along the gray dashed line and must cross the black dashed line in order to record a first-passage time event. (B) A heat-map of MFPT in units of minutes as a function of cell-ECM adhesion energy, β and polarization bias strength, ϵ. Warmer colors represent higher MFPT values (colorbar). Parameter values for the heat-map: $N = 20$, $\bar{c} = 10\text{nM}$, $g = 0.004\text{nM}/\mu\text{m}$, $\Gamma = 80(\mu\text{m min.})^{-1}$. Illustrations in (C) represent cluster migratory behavior in their respective regimes of parameter space. Larger values of ϵ correspond to larger cell polarization vectors (red arrows), whereas larger values of β correspond to an ECM that is more difficult to traverse. (D) Mean cluster size $\langle N_{\text{sub}} \rangle$ as a function of the total number of cells in the system N. Regime 1: $\beta = 1.5$, $\epsilon = 1.0$. Regime 2: $\beta = 3.5$, $\epsilon = 0.8$

were calibrated using the cluster migration data from Malet-Engra et al. [52] and assuming a typical cell radius $a = 10\mu\text{m}$. Similar to the experimental study, initial simulations were conducted with a gradient and background concentration equivalent to $\bar{g} = 0.001\text{nM}/\mu\text{m}$ and $\bar{c} = 1\text{nM}$. We found that increasing the gradient and background concentration values to those reported in Table 3.1 (see pg. 11), which still maintain the limit $a\bar{g} \ll \bar{c}$, decreased computation cost while yielding the same qualitative results. Therefore all results presented here use the values of $\bar{c}$ and $\bar{g}$ in Table 3.1. The simulation timescale was then calibrated such that clusters of cells migrate with velocities on the same order as those in the study by Malet-Engra et al. All simulation parameter values used are presented and motivated in Table 3.1 unless specified otherwise.

In order to quantify model behavior, statistics on the simulated mean first-passage time (MFPT) for migrating clusters are collected. The first-passage time is the time it takes for the center of mass of a cluster of cells to cross a threshold distance. First it is important to understand the effects of the various parameters in our model on simulations results. Across simulations, two crucial parameters emerge: β the cell-ECM adhesion energy, and ϵ the polarization bias strength. When these two parameters are varied three distinct phases of collective cell migration are clear (regimes 1, 2, and 3 in Fig. 3.2B).

Fig. 3.2B shows that for sufficiently large β the mean first-passage time remains relatively constant as β and ϵ grow in proportion to one another. In this phase, regime 2 of Fig. 3.2B, cells migrate as a collective as illustrated in Fig. 3.2C. However if the adhesion energy is further increased while the bias strength remains fixed the MFPT starts to increase (regime 3 of Fig. 3.2B). This is due to the increased energy cost in cells making protrusions into the ECM. If β is increased further the cluster cells will eventually stop moving since protrusions become highly improbable as dictated by the CPM (Fig. 3.2C). The other large MFPT phase is due to increasing ϵ while keeping β fixed (regime 1 of Fig. 3.2B). In this case the cell's polarization becomes large enough to overcome the intercell adhesion energy causing the cluster of cells to scatter as illustrated in Fig. 3.2C. To further characterize whether a cluster will scatter or remain persistently connected, we track the mean subcluster size $\langle N_{\text{sub}} \rangle$, defined as the average cluster size weighted by the number of cells present in each constituent cluster (Fig. 3.2D). Although cells' initial configuration is that of a single cluster, partial scattering may occur stochastically and reversibly, leading to a value of $\langle N_{\text{sub}} \rangle$ that is less than the cluster size N. As seen in Fig. 3.2D, the persistence $\langle N_{\text{sub}} \rangle / N$ is largely independent of N, and clusters in the parameter space of regime 2 are more persistent than those corresponding to regime 1 where cells are likely to scatter permanently. Overall, we see that there is a large region in parameter space which yields physically realistic behavior, and the model breaks down in the limits
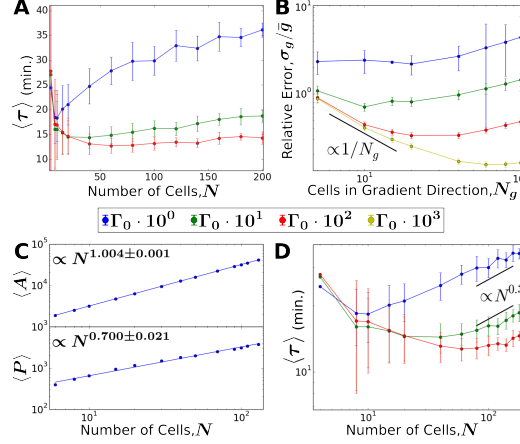
Fig. 2.3. Tradeoff between sensing and drag leads to a minimum mean first-passage time (MFPT) with cluster size. $\Gamma_0 = 0.80(\mu m\ min)^{-1}$. (A) MFPT for various values of the exchange rate per unit contact-length Γ. (B) Relative error in gradient sensing for various values of Γ. (C) Area A and perimeter P scaling relationships with the number of cells N in a cluster. (D) MFPT results in A on a log-log scale, compared with the geometric prediction arising from C. All error bars represent standard deviation.

where we would expect it to. With this in mind we further examine simulations within regime 2 of parameter space.

Next we examine the MFPT as a function of cluster size (Fig. 3.3A). Starting from $N = 2$ we see that for sufficiently large Γ (red curve), as the number of cells increases the MFPT decreases. This can be understood from our description of multicellular sensing (Eq. 3.2): before reaching the critical number of cells in a cluster, the error in gradient sensing decreases as $\sigma_R/\bar{R} \sim N^{-1}$ and so the cluster's ability to more precisely measure the gradient increases. The decreased sensing error translates into more accurately directed cell polarization vectors causing the MFPT to decrease. Fig. 3.3B shows the relative error vs. the number of cells in the cluster that are parallel to the gradient direction, N_g. In the small-cluster regime and for fast communication (yellow curve) there is a decrease in relative error with N_g, that is in close agreement with the theoretical prediction for the scaling of N_g^{-1} (Eq. 3.2). Since the global-

reporter exchange rate between cells is very large compared to the degradation rate ($\gamma \gg \mu$) it is expected that the effects of communication can be neglected as was the case in deriving Eq. 3.2. However, as the cluster grows in size the effects of communication can no longer be neglected. As illustrated in Fig. 3.3B the relative error reaches a lower limit as predicted by Eq. 3.4 at which sensory precision will no longer increase with increased cluster size.

As the number of cells increases the MFPT tends to saturate to a minimal value and may even begin to increase (Fig. 3.3A). The MFPT reaches a minimum around $N \sim 10-100$ cells depending on the choice of Γ, the global molecule exchange rate per unit contact-length. Communication between cells improves as Γ increases since more Y molecules can be quickly transmitted between cells, pushing the point of saturation to larger cluster sizes. From these results we see that the model predicts an optimal cluster size for fastest migration. This prediction is in contrast with similar studies which in some cases predict a saturation in velocity and therefore constant MFPT as a function of cluster size [41, 52]. The dependence of MFPT on cluster size is further explored in the Discussion.

In the limit that $\Gamma a/\mu \lesssim 1$ (a being the cell radius) intercellular communication within the cluster is highly localized, and increasing the size of the cluster will not improve sensory precision. If this is the case then the cluster will have outgrown its optimal size for gradient detection. Instead of the cluster acting as one cohesive gradient-sensing device the cluster will comprise several independent gradient sensors which cannot reliably share information with one another. Therefore, in the small Γ limit we expect the MFPT to monotonically increase with increasing N due to increased drag on the cluster. Indeed, simulation results confirm our expectations in the large N, small Γ limit (Fig. 3.3A, blue curve).

Next we asked if the MFPT had any dependence on the geometrical properties of the migrating clusters [68]. The mean first-passage time should scale proportionally

with the drag experienced on the cluster, whereas it should be inversely related to the force driving migration,

$$\langle \tau \rangle \sim \frac{\text{drag}}{\text{force}}. \tag{2.16}$$

The drag on the cluster should scale with the area of the cluster, drag $\propto A(N)$, and the driving force should scale with the perimeter of the cluster since we know that only cells on the edges of the cluster are polarized in the desired direction, force $\propto P(N)$. Although the size and shape of clusters will fluctuate we can obtain from many simulations how the average area $\langle A \rangle$ and perimeter $\langle P \rangle$ scale with N. Fig. 3.3C shows that both scale with powers of N, i.e. $\langle A \rangle \sim N^d$ and $\langle P \rangle \sim N^f$. We find $d = 1.004 \pm 0.001$, which makes sense since the average area of the should scale linearly with the number of cells. We also find $f = 0.700 \pm 0.021$, which is intriguing because for a circular cluster we would expect $f = 1/2$. The larger value of f reflects the elongated and amoebic shape of the cluster (Fig. 3.2A), which causes its perimeter-to-area ratio to be larger than that expected for a circle.

Given these geometric scalings, Eq. 3.16 then makes a prediction: the MFPT should scale as $\langle \tau \rangle \sim N^{d-f} = N^{0.304 \pm 0.021}$. We compare this prediction to the MFPT data, on a log-log scale, in Fig. 3.3D. We see that in the large N, small Γ limit, the prediction agrees well with the data (blue and green curves). This demonstrates that the slowdown of large, poorly communicating clusters is dominated by the geometrical aspects of cluster propulsion and drag.

In summary, in the limit that communication between cells is strong ($\Gamma a/\mu \gg 1$), information can be reliably transferred over $n_0 \gg 1$ cells. As long as cluster sizes N remain smaller than n_0 cells, there will be an improvement in the sensory capability of the cluster with size, and an associated decrease in the MFPT $\langle \tau \rangle$. As the critical size n_0 is reached, sensory ability will cease to improve with size, and $\langle \tau \rangle$ will reach a minimum. Further addition of cells will cause $\langle \tau \rangle$ to increase according to $\langle \tau \rangle \sim$ drag/force, since the drag is proportional to the cluster area, whereas the force is proportional only to the cluster perimeter.

2.3 Discussion

We have developed a model in which collective sensing of noisy chemical gradients induces multicellular migration. The model includes the stochastic processes of ligand diffusion, intercellular communication and cell shape fluctuations. In the model cells are polarized based on collective gradient information and contact-mediated interactions, leading to biased migration despite the fact that individual cells do not chemotax. We find that the antagonistic effects of sensing and drag result in a minimum mean first-passage time (MFPT) as a function of cluster size, i.e. an optimal size for fastest migration. The optimal size is governed by the strength of cell-cell communication, with stronger communication leading to both a larger optimal size and a decreased migration time (Fig. 3.3D).

Whereas previous models have idealized cell or cluster geometries as perfect circles [41, 68], our use of the cellular Potts model has allowed us to capture natural fluctuations in cell and cluster shape. As a result, we have found that while migrating, clusters adopt a shape that is (i) elongated in the gradient direction and (ii) non-convex (see Fig. 3.2A). Both features lead to a cluster perimeter-to-area ratio that is significantly larger than that expected for a circle or other convex shape with aspect ratio near unity. Importantly, we have found that the area and perimeter scalings remain predictive of MFPT in the communication-limited regime (Fig. 3.3D), even with the observed non-circular and fluctuating geometries.

To the extent possible, our model has been constructed and parameterized using current experiments on collective migration. Intercellular communication is modeled as a direct exchange of messenger molecules between cells since this type of communication has been implicated in development, organoid branching, angiogenesis, and cancer [6, 59–62]. The chemical concentration and gradient values are selected to ensure that our simulations are in the shallow gradient regime, where experiments show that collectives can respond whereas single cells cannot [6, 7, 52]. Cell size, chemical concentration, chemical gradient, cell-cell contact energy, and cell-ECM contact en-
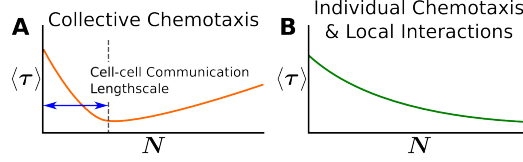
Fig. 2.4. Prediction to distinguish collective from individual chemotaxis in experiments. (A) Expected MFPT behavior for cluster migration driven by collective sensing. (B) Expected MFPT behavior for cluster migration driven by local interactions.

ergy values are taken from previous experimental studies of collective cell behavior (Table 3.1).

How do our model predictions compare to experiments? There have been many studies on collective migration [13, 26, 57, 59] though only one (to our knowledge), by Malet-Engra et al. [52], measures migratory properties as a function of cluster size. The experiments conducted by Malet-Engra et al. reveal that beyond a minimum cluster size, the cluster velocity saturates to a maximal value and then remains constant with increasing cluster size. In our study, we find that when communication is strong, the MFPT – which is inversely related to the mean velocity – also saturates to a minimal value and remains constant for a large range of cluster sizes. As shown in Fig. 3.3A (red curve), as the cluster size increases from about 30 to 200 cells the MFPT remains relatively constant, in qualitative agreement with the aforementioned experimental results. This saturation regime occurs when communication is sufficiently strong to suppress, over a large range of cluster sizes, the drag-induced slowdown. Our findings thus suggest that sensory information is reliably transferred throughout the clusters of lymphocytes studied by Malet-Engra et al., and that communication is strong enough that drag does not strongly constrain migration speed for the cluster sizes analyzed.

Furthermore, our results suggest a simple experimental test that can distinguish whether cluster chemotaxis is purely collective or individually driven. Broadly speaking, cluster migration (i) can emerge collectively from cells that communicate, either

chemically or mechanically, but do not chemotax alone (as in our model), or (ii) it can result from many individual agents that take independent measurements of the environment and through physical coupling or local interactions produce collective migration [40, 69] (a so-called "many wrongs" mechanism [39]). As illustrated in Fig. 3.4A, our results suggest that in the former case, one would observe a minimum in the migration time as a function of the cluster size, with the optimal size determined by the length scale of collective information processing within the cluster. In contrast, as illustrated in Fig. 3.4B, in the latter case migration is driven by the integrated measurements of many effectively independent agents, and thus one would observe a monotonic decrease in the migration time as a function of the cluster size [39]. Distinguishing the dependence in Fig. 3.4A from that in Fig. 3.4B using microscopy would provide phenomenological evidence of purely collective chemotaxis without relying on molecular-level details.

An important feature of our model and its analysis is that the timescale of sensing is faster than the timescale of cell response and motility (Table 3.1). However, in actuality the duration of cells' sensing timescales relative to their response timescales is unknown [6]. If the motility timescale is shorter than that of sensing for a specific cell type than the MFPT dependence on cluster size may be more complicated than predicted. For short response timescales we expect migratory behavior to be more strongly diffusive, but to still remain biased in the direction of the gradient over periods of time larger than the sensing timescale.

In our model, the precision of multicellular migration is determined in part by noise arising from ligand diffusion at the initial sensory stage. As such, the model respects the fundamental limits to the precision of collective gradient sensing set by the physics of diffusion, which were recently tested in collectives of epithelial cells [6,8]. It will be interesting to see how these and similar limits translate from the domain of sensing to that of migration, and whether they depend on the underlying migration mechanism (purely collective, individually driven, or a mixture thereof).

3. LIMITS TO COLLECTIVE CHEMOTAXIS

Collective migration is ubiquitous in cell biology, occurring in organism development [53, 70–72], tissue morphogenesis [6] and metastatic invasion [19, 62, 73, 74]. Collective migration often occurs in response to chemical cues in the environment, a process known as chemotaxis. The simplest way for cells to collectively chemotax is by individual detection and response to the chemical attractant: each cell measures the spatial difference in chemoattractant across its body and moves in the perceived direction of the gradient, while short-range coupling keeps the group together. Groups performing this type of *individual-based chemotaxis* (IC) are found not only in cell biology [75] but also in ecological systems such as bird flocks [39]. However, recent experiments have uncovered an alternative type of chemotaxis, in which cells grouped together chemotax differently than if they were alone [21, 52, 58, 76]. For example, outer cells may polarize while inner cells do not, a mechanism observed in neural crest cells [53] and considered in several recent modeling studies [41, 52, 77]. This type of *emergent chemotaxis* (EC) behavior seen in cell collectives presupposes a machinery within cells which allows for behavior to change once a cell is in a group. Since this machinery may come at a cost, this raises the question of whether EC offers any fundamental advantage over IC.

We address this question using simple physical models of EC and IC. Cell collectives respond to graded profiles of freely diffusing molecules, and we quantify the migratory behavior of one-dimensional (1D) cell chains, two-dimensional (2D) cell sheets, and three-dimensional (3D) cell clusters [Fig. 4.1(a)], configurations designed to mimic physiological multicellular structures such as filaments and ducts [13, 62, 78]. Collectives performing EC and IC are found to have very similar mean speed, with polarization strength scaling linearly with the number of cells regardless of chemotactic mechanism or dimensionality. However, 1D and 2D EC collectives have higher
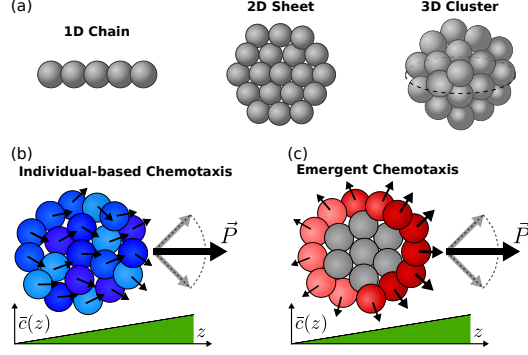
Fig. 3.1. (a) We study the chemotactic performance of 1D chains, 2D sheets, and 3D clusters of cells. (b) In individual-based chemotaxis (IC), cells in the collective polarize based on their own gradient measurement. (c) In emergent chemotaxis (EC), cell polarization depends on intercellular interactions: cells on the edge polarize based on their measurement of the concentration, and cells in the bulk do not polarize. In both mechanisms the total polarization $\vec{P}$ will fluctuate in magnitude and direction due to noise in cell measurements.

chemotactic precision than IC collectives: we find that for N cells, the relative error in EC scales as $\{N^{-2}, N^{-3/2}, N^{-1}\}$ for 1D, 2D, and 3D, respectively, whereas in IC it scales as N^{-1} for any dimension. We explain the physical origin of this difference and discuss its implications.

We first consider IC [Fig. 4.1(b)]. Due to the chemoattractant molecules in the environment, each cell i becomes polarized with vector $\vec{p}_i$ in its desired direction of motion [31]. The components of $\vec{p}_i$ reflect the difference in concentration $c(\vec{r}, t)$ between the front and back of the cell in each respective direction. This concentration difference will fluctuate due to the particulate nature of diffusion. Focusing on this extrinsic source of noise, we treat each cell as a sphere of radius a through which molecules freely diffuse, akin to the "perfect instrument" described by Berg and Purcell [2]. The concentration difference is encoded internally as a weighted count of the molecules within the cell volume U_i. The weighting function will depend on the sensory network, but will generally be positive at the front and negative at the back;

here we choose cosine for simplicity. Orienting our coordinate system such that $\hat{z}$ is parallel to the gradient, the components of $\vec{p}_i$ become

$$p_{i\alpha}(t) = \int_{U_i} d^3r \ w_\alpha c(\vec{r}, t), \tag{3.1}$$

where $\alpha \in \{x, y, z\}$, and in spherical coordinates the cosine is $w_\alpha = \{\sin\theta\cos\phi, \sin\theta\sin\phi, \cos\theta\}$. The concentration is a random variable of the form $c(\vec{r}, t) = c(0, t) + \vec{r} \cdot \vec{g}(\vec{r}, t)$, which obeys regular diffusion $\dot{c} = D\nabla^2 c + \eta_c$ with D the diffusion coefficient and η_c the Langevin noise due to the diffusive fluctuations in concentration [79, 80]. The mean concentration is $\bar{c}(\vec{r}) = c_0 + \vec{r} \cdot \vec{g}$, and first we consider a constant gradient $\vec{g} = g\hat{z}$ that is shallow ($ag \ll c_0$). Cells are assumed to preferentially adhere to one another, hence the polarization of a collective of N cells is the sum of its constituent cells' polarization vectors $\vec{P}(t) = \sum_{i=1}^{N} \vec{p}_i(t)$.

The collectives exist at low Reynolds number, hence their velocity $\vec{v}$ is proportional to the motility force, and in turn the polarization $\vec{P}$. Therefore, understanding the behavior of $\vec{P}$ will inform us of the collective migratory performance. We focus on two measures of performance: the mean and the relative error of the polarization in the gradient direction P_z, where the relative error is defined

$$\epsilon^2 = \frac{\text{Var}[P_z]}{\langle P_z \rangle^2} = \frac{\text{Var}[v_z]}{\langle v_z \rangle^2}. \tag{3.2}$$

To investigate $\langle P_z \rangle$ and ϵ^2 for the IC model, we first perform particle-based simulations of the chemoattractant in the presence of the permeable cells [81, 82]. We find that the total mean polarization $\langle \vec{P} \rangle$ points solely in the gradient direction with equal magnitude regardless of dimensionality [Fig. 4.2(a), blue data points]. Indeed, Eq. 4.1 indicates that a single cell will have mean polarization proportional to the concentration difference across the cell, $\langle \vec{p}_i \rangle = \pi a^4 g\hat{z}/3$, regardless of the cell's location. Therefore the mean collective polarization is geometry-independent, depending only on the number of cells present,

$$\langle \vec{P} \rangle_{\text{IC}} = \frac{\pi}{3} a^4 g N \ \hat{z}, \tag{3.3}$$

as shown in Fig. 4.2(a) (blue lines).
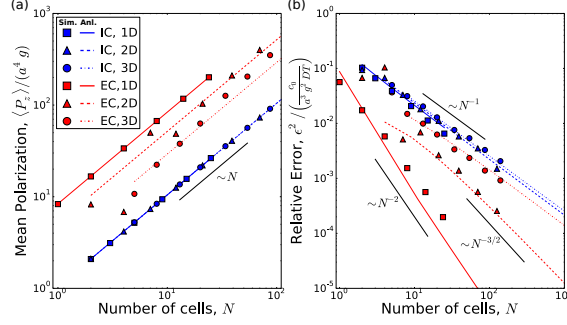
Fig. 3.2. (a) Mean cluster polarization and (b) relative error for both mechanisms of collective chemotaxis in every configuration. Points are simulation data, colored lines are analytical predictions. 1D EC data plotted with respect to $N - 1$.

We next investigate the relative error for IC collectives. Simulations show that the error decreases with cluster size as $\epsilon^2 \sim N^{-1}$ for all three geometries [Fig. 4.2(b), blue data points]. Indeed this is the result that one would obtain if the cells were independent sensors [39]. However, they are not independent: their noise is correlated by fluctuations in the concentration [8, 80]. To understand why correlations do not affect the relative error we investigate the model analytically.

We linearize the concentration $c(\vec{r}, t) = \bar{c}(\vec{r}) + \delta c(\vec{r}, t)$ as well as the cell polarization $\vec{p}_i(t) = \langle \vec{p}_i \rangle + \delta \vec{p}(t)$, and by Fourier transforming in both space and time we derive analytic expressions for $\text{Var}[P_z]$ and thereby ϵ^2 [81]. Since $P_z = \sum_{i=1}^{N} p_{iz}$, the variance in the total polarization is a linear combination of all cell polarization variances and covariances present in the collective,

$$\text{Var}[P_z] = \sum_i \text{Var}[p_{iz}] + \sum_{i \neq j} \text{Cov}[p_{iz}, p_{jz}] \equiv V + C, \tag{3.4}$$

The variance and covariance for cells within the collective are derived from the power spectrum in polarization cross correlations, taking the general form

$$\text{Cov}[p_{i\alpha}, p_{j\alpha}] = \frac{1}{T} \lim_{\omega \to 0} \int \frac{d\omega'}{2\pi} \langle \delta \tilde{p}_{i\alpha}^*(\omega') \delta \tilde{p}_{j\alpha}(\omega) \rangle , \tag{3.5}$$

with T the cell's measurement integration time and $\text{Var}[p_{i\alpha}] = \text{Cov}[p_{i\alpha}, p_{i\alpha}]$ [3, 8, 80]. Eq. 4.5 assumes that the integration time is larger than the timescale of molecule

diffusion over the radius R of the collective, $T \gg \tau_D = R^2/D$, though we relax this assumption in later simulations. Following this procedure we find that V and C for IC are [81]

$$V_{\text{IC}} = \frac{4\pi a^5 c_0}{45DT} N,$$
(3.6)

$$C_{\text{IC}} = -\frac{\pi a^5 c_0}{18DT} \sum_{i \neq j}^{N} \frac{3\cos^2 \Theta_{ij} - 1}{n_{ij}^3}.$$
(3.7)

Here n_{ij} is the number of cell radii separating the centers of cells i and j, and Θ_{ij} is the angle between the gradient direction and a line connecting the two cells.

V_{IC} scales with N since each cell is involved in gradient sensing. However, Eq. 4.7 reveals an angular dependence on the correlations between two IC cells. A pair of cells can be correlated or anti-correlated depending on their locations relative to the gradient. For example, if a pair of cells is parallel to the gradient then $\cos^2 \Theta_{ij} = 1$, resulting in a negative covariance, indicating that their gradient measurements are anti-correlated. In contrast, if two cells are perpendicular to the gradient then $\cos^2 \Theta_{ij} = 0$, resulting in a positive covariance and correlations between the two cells. The resulting contribution of C_{IC} to $\text{Var}[P_z]$ is dimensionality-dependent since the angles made between pairs of cells is determined by geometry, whereas V_{IC} is dimension-independent.

For a 1D chain of IC cells, every pair is parallel to the gradient resulting in anti-correlated measurements which we find in total scale as N [81]. As dimensionality increases, more and more pairs of cells will be perpendicular to the gradient resulting in reduced anti-correlations in the collective. This culminates in 3D clusters having zero cell-cell covariance contribution to the total cluster variance [81]. This results in $\epsilon^2 \sim N^{-1}$ regardless of dimensionality, indicating that IC cells behave as effectively independent gradient sensors, even with diffusion-mediated cross-correlations. The scalings for V and C are summarized in Table 4.1. The resulting ϵ^2 predictions are plotted in Fig. 4.2(b) (blue lines), and we see excellent agreement with the simulations.

Next we turn our attention to EC, the mechanism in which grouped cells sense and migrate differently than individuals. Often cells in a cluster differentiate, with

		$\langle P_z \rangle$	V	C	ϵ^2
IC	1D	N^1	N^1	$-N^1$	N^{-1}
	2D	N^1	N^1	$-N^1$	N^{-1}
	3D	N^1	N^1	0	N^{-1}
EC	1D	N^1	N^0	$-N^{-1}$	N^{-2}
	2D	N^1	$N^{1/2}$	$N^{1/2}$	$N^{-3/2}$
	3D	N^1	$N^{2/3}$	N^1	N^{-1}

Table 3.1.
Summary of scaling behavior. N dependence of the leading order term for the mean $\langle P_z \rangle$, and the variance (V) and covariance (C) contributions to the relative error $\epsilon^2 = (V + C)/\langle P_z \rangle^2$. C for EC in 2D has a log correction [81].

edge cells polarized and bulk cells unpolarized [52, 70]. In accordance with previous studies [41, 77], we assume that cell interactions are mediated by contact inhibition of locomotion [42]. The interactions result in edge cells polarized away from their neighbors, and interior cells that remain uninvolved in chemical sensing and do not polarize [Fig. 4.1(c)]. The edge cells polarize with strength proportional to the local concentration which, again like Berg and Purcell's perfect instrument [2], is estimated by counting the molecules present within their cell volume. Hence we define the polarization of the ith cell in the collective as

$$\vec{p}_i(t) = \begin{cases} \hat{r}_i \int_{U_i} d^3r \; c(\vec{r}, t) & i \in \{N_{\text{edge}}\} \\ 0 & i \in \{N_{\text{bulk}}\} \; , \end{cases} \tag{3.8}$$

where $\hat{r}_i$ points radially outwards from the collective. Eq. 4.8 dictates that $\vec{p}_i$ is dependent on a cell's location relative to the collective. As illustrated in Fig. 4.1(c), only

the cells on the edge sense the chemoattractant, polarizing with a larger magnitude on the high concentration side of the collective, and the total polarization depends only on the cells along the edge: $\vec{P} = \sum_i \vec{p}_i$, $\forall i \in \{N_{\text{edge}}\}$.

Simulations for EC show that the mean polarization $\langle P_z \rangle$ scales with N for all geometries [Fig. 4.2(a), red points] even though N_{edge} is dependent on the dimensionality of the collective. Our analytical solution helps us understand this result. For 1D EC, only the two opposing cells are polarized so $\langle \vec{P} \rangle$ can be solved for exactly, but for 2D and 3D we take the continuum limit of $\vec{P} = \sum_i \vec{p}_i$, assuming the collective is much larger than a single cell $R \gg a$ [81]. The resulting expressions are

$$\langle \vec{P} \rangle_{\text{EC}} = f_d a^4 g N \ \hat{z}, \tag{3.9}$$

where the prefactors are $f_d = \{8\pi/3, 2\pi^2/3, 16\pi/9\}$ for $d = \{1, 2, 3\}$ dimensions, and for $d = 1$ we have taken $N - 1 \to N$ for large N. Eq. 4.9 is shown in Fig. 4.2(b) (red lines), and we see good agreement. $\langle P_z \rangle$ scales with N because it depends on the product of $N_{\text{edge}} \sim N^{(d-1)/d}$ and the distance spanned in the gradient direction $R \sim N^{1/d}$, resulting in a mean polarization which is geometry invariant [52].

Comparing EC and IC shows that $\langle P_z \rangle \sim N$ regardless of collective migration mechanism or geometry as seen in Fig. 4.2(a). $\langle P_z \rangle$ has the same parameter dependency for both EC and IC, namely $a^4 g$, which is the average change in the number of chemoattractant molecules across a cell. Although $\langle P_z \rangle_{\text{EC}} \approx 6 \langle P_z \rangle_{\text{IC}}$ meaning that EC speed is faster than IC, this relatively small difference may be difficult to detect in biological systems. Moreover, both mechanisms have the same N scaling. Does the same equivalence between EC and IC also hold for the relative error?

Interestingly, simulations show that the EC relative error does depend on geometry and in fact outperforms IC in terms of scaling in 1D and 2D [Fig. 4.2(b), red points]. Only in 3D does the relative error appear to scale the same as IC. In order to understand the dimension dependence of the EC relative error we again investigate

the model analytically. Following the procedure outlined by Eqs. 4.4 and 4.5 we find analytic expressions for $\text{Var}[P_z] = V + C$ for EC [81],

$$V_{\text{EC}} = \frac{16\pi a^5 c_0}{15DT} \sum_{i=1}^{N_{\text{edge}}} \cos^2 \Theta_i, \tag{3.10}$$

$$C_{\text{EC}} = \frac{8\pi a^5 c_0}{9DT} \sum_{i \neq j}^{N_{\text{edge}}} \frac{\cos \Theta_i \cos \Theta_j}{n_{ij}}, \tag{3.11}$$

with Θ_i the angle $\hat{r}_i$ makes with the gradient. Both V_{EC} and C_{EC} depend on dimensionality simply because $N_{\text{edge}} \sim N^{(d-1)/d}$. From Eqs. 4.10 and 4.11 we see that $V \sim N_{\text{edge}}$, and that C depends on the angles edge cells make with the gradient. The angular dependence means that cells along the front and back sides of the cluster (relative to the gradient) are strongly anti-correlated since $\cos \Theta_i \cos \Theta_j \approx -1$, whereas pairs of edge cells near the middle are very weakly correlated ($\cos \Theta_i \cos \Theta_j \approx 0$). Unlike in the case of IC, the scaling of C with N increases with dimensionality [81] as summarized in Table 4.1, and the resulting ϵ^2 predictions show good agreement with the simulation results [Fig. 4.2(b)].

The dimension dependence of the EC relative error can be understood by thinking of the collective as one large detector whose sensory surface is comprised of two halves. If both halves were to take measurements of their local concentrations and then polarize in opposing directions with strengths proportional to their measurements, then ϵ^2 would depend on the size of each half a_{eff} and their separation distance A_{eff} according to $\epsilon^2 \sim a_{\text{eff}}^{-1} A_{\text{eff}}^{-2}$ [8]. The size of each half is independent of N for a 1D chain (each half is a single cell), but it scales as $a_{\text{eff}} \sim N^{1/d}$ for $d = 2$ or 3 dimensions. The separation distance scales with the radius of the collective for all d, $A_{\text{eff}} \sim N^{1/d}$. This results in $\epsilon^2 \sim \{N^{-2}, N^{-3/2}, N^{-1}\}$ for $d = \{1, 2, 3\}$ [Fig. 4.2(b), black lines], which agree with the scalings seen in simulations and analytics.

Thus, the physical origin of the advantage of EC over IC lies in how the errors scale with the collective size N. In IC, all N cells contribute to the sensing, and cross-correlations between them scale either linearly or sublinearly with N, leading to a scaling $\epsilon \sim 1/\sqrt{N}$ that is characteristic of independent sensors. But in EC,

only $N_{\text{edge}} \sim N^{(d-1)/d}$ cells contribute to the sensing, leading to a sublinear scaling with N of the variance contributions of the individual cells. The total variance of the collective, then, depends on the cross-correlations, which are geometry-specific: in 1D they are dwarfed by the individual variances, in 2D they are commensurate, and in 3D they dominate (Table 4.1). As a result, 1D and 2D EC collectives benefit from a variance that scales subextensively, i.e., sublinearly with N.

Our analytical treatment relies on several assumptions which we now relax using the simulations. In Fig. 4.2 the integration time T is larger than the timescale for molecule diffusion τ_D. We find that reducing T to as much as two orders of magnitude smaller than τ_D still results in the expected relative error scalings, with 1D and 2D EC outperforming IC [81]. Similarly, using an exponential concentration profile instead of a linear one does not change the relative error scaling behavior [81].

In our model, IC polarization is adaptive to the background concentration as observed in the Ras signalling pathway for *Dictyostelium discoideum* chemotaxis [83]. On the other hand, our EC model is non-adaptive. Cell polarization increases with background concentration causing tension in the collective [Fig. 4.1(c)], as previously studied [41]. However, adaptive collective sensing has been observed in mammary epithelial cells [6]. Our EC model could be made adaptive by replacing the integrand in Eq. 4.8 with $c(\vec{r} + \vec{r}', t) - c_0$. This change does not affect the properties of $\vec{P}$ since the background concentration cancels out when summing over all edge cells, but it does remove the internal tension in the collective.

Besides the advantage revealed here in terms of chemotactic precision, another benefit of EC is in terms of cell differentiation. In EC only edge cells need to be involved in chemical sensing and polarization, freeing bulk cells from the obligation of receptor and protein production necessary for chemotaxis. Bulk cells are free to differentiate into other phenotypes, possibly serving different uses for the collective. This is in stark contrast with IC where every cell must be of the polarized phenotype, leaving no cells with the freedom to differentiate.

The two EC advantages of improved chemotactic precision and the possibility of cell differentiation may be why EC-style collective migration is more prevalent than IC. For example, EC has been observed in two dimensional collectives of malignant lymphocytes [52] and in border cell migration [70]. In cancer, metastatic invasion sometimes occurs in the form of chains of cells leaving the tumor with a leader cell at the front [13, 62], analogous to our 1D EC model. Two-dimensional EC migration may also be implicated in tumorigenesis and metastasis in pancreatic ductal cells given the cylindrical surface-like geometry of pancreas ducts [78].

How can our predictions be tested in experiments? The chemotactic index (CI), commonly defined as $\text{CI} \equiv \langle \cos\theta \rangle$ where θ is the angle between the trajectory and the gradient [35], is actually a simple monotonic function of ϵ^2. For small deviations from perfect chemotaxis, we have $\text{CI} \approx 1 - \langle \theta^2 \rangle / 2 = 1 - \text{Var}[\theta]/2$. If v_z and v_x are the components of the velocity of the collective parallel and perpendicular to the gradient, respectively, then $\theta \approx v_x/v_z$ with $\langle v_z \rangle > 0$ and $\langle v_x \rangle = 0$, resulting in $\text{Var}[\theta] = \text{Var}[v_z]/\langle v_z \rangle^2 = \epsilon^2$. Therefore the relative error and chemotactic index are related as $\text{CI} = 1 - \epsilon^2/2$ for small errors. With this relationship the predicted scalings of ϵ^2 for EC and IC may be tested with chemotaxis experiments. Additionally, the CI scaling behavior could be used to determine whether an EC- or IC-style migration is at play in an unknown system.

We have shown how the fluctuations in a diffusing attractant concentration set physical limits to collective chemotactic performance. By focusing on two fundamental classes of collective chemotaxis, we have found that the mean speed scales with the size of the collective irrespective of the mechanism or geometry, but that an emergent mechanism outperforms an individual-based one for 1D and 2D geometries in terms of chemotactic precision. This advantage arises due to the ways that errors accumulate in the two mechanisms: in an emergent strategy, fewer cells contribute their sensory noise to the collective, and in 1D and 2D the cross-correlations between cells remain low, ultimately leading to a subextensive scaling of polarization variance with collective size. As such, the performance advantage is an inherent property of the

emergent mechanism, and we suspect that it not only helps explain the prevalence of emergent chemotaxis in cellular systems, but that it also is detectable using standard measures such as the chemotactic index.

Supplementary Information for
"Emergent versus Individual-based Multicellular Chemotaxis"

3.1 Particle-based Simulations

We perform computational simulations in order to test the properties of EC and IC for one, two and three dimensional collectives. In the simulation, particles move randomly inside a 3D volume and boundaries are set to produce the desired concentration profiles. Cells are placed at fixed positions in the 3D volume in either one, two or three dimensional configurations. For a linear concentration profile, one boundary produces particles, and the opposing one is an absorbing boundary while all other boundaries periodic. For an exponential concentration, the same boundaries are used and particles are also allowed to degrade.

At each time-step of the simulation particles randomly move and are produced. In a given time-step particles move in a random direction with a probability $p = D\Delta t/b^2$, with b the particle hopping distance, D the diffusion coefficient, and Δt the time-step. A particle is produced during that time-step with probability $q = k\Delta t$, with k the production rate. The time-step Δt is set such that $p + q \leq 1$. In the case of an exponential concentration profile, particles may also degrade during a time-step. Particles degrade with probability $r = \beta\Delta t$, with β the degradation rate. In this case Δt is set such that $p + q + r \leq 1$.

The simulation code used for this paper can be found at `https://doi.org/10.5281/zenodo.401040`, and the most up-to-date version of the code can be found at `https://github.com/varennes/particletrack`.

3.2 Analytic Results

We consider collectives in one, two and three dimensions of radius R comprised of N cells. Each cell is taken to be a permeable sphere of radius a through which

molecules of the surrounding chemical concentration $c(\vec{r}, t)$ can freely diffuse. The chemical concentration is taken to be

$$c(\vec{r}, t) = c(0, t) + \vec{r} \cdot \vec{g}(\vec{r}, t) \tag{3.12}$$

with $\vec{g}$ parallel to the z axis. The chemical concentration obeys normal diffusion

$$\dot{c} = D\nabla^2 c + \eta_c \tag{3.13}$$

with D the diffusion coefficient, and η_c the Langevin noise due to fluctuations in concentration. We linearize the concentration $c(\vec{r}, t) = \bar{c}(\vec{r}) + \delta c(\vec{r}, t)$ with

$$\bar{c}(\vec{r}) = c_0 + \vec{r} \cdot \vec{g} \tag{3.14}$$

where c_0 is the mean concentration at the origin. The Langevin noise term η_c, and the Fourier transformed fluctuation in the concentration $\delta\tilde{c}(\vec{k}, \omega)$ have the following properties (see Ref. [23] of the main text):

$$\langle \tilde{\eta}_c(\vec{k}', \omega')\tilde{\eta}_c(\vec{k}, \omega) \rangle = 2D \; 2\pi\delta(\omega - \omega') \int d^3 y \; \vec{k} \cdot \vec{k}' \; \bar{c}(\vec{y}) \; e^{i\vec{y} \cdot (\vec{k} - \vec{k}')} \;, \tag{3.15}$$

$$\langle \delta\tilde{c}(\vec{k}', \omega')\delta\tilde{c}(\vec{k}, \omega) \rangle = \frac{\langle \tilde{\eta}_c(\vec{k}', \omega')\tilde{\eta}_c(\vec{k}, \omega) \rangle}{(Dk^2 - i\omega)(Dk'^2 + i\omega')} \;. \tag{3.16}$$

Next, we define the cell polarization vectors for individual-based chemotaxis (IC) and emergent chemotaxis (EC). Collectives of N cells form shapes of different dimensionality: a chain of cells of length $2R$ (1D), a disc of cells with radius R (2D), and a sphere of cells of radius R (3D).

3.2.1 Individual-based Chemotaxis

In the IC mechanism, cells independently measure the chemoattractant gradient in order to set their polarization vector $\vec{p}$. For a spherically-shaped cell with volume U_i, $\vec{p}_i$ is defined as

$$p_{i\alpha}(t) = \int_{U_i} d^3 r \; w_\alpha c(\vec{r}, t), \tag{3.17}$$

where $\alpha \in \{x, y, z\}$, and in spherical coordinates the cosine is $w_\alpha = \{\sin\theta\cos\phi, \sin\theta\sin\phi, \cos\theta\}$. The x, y, z components are written as

$$p_{ix}(t) = \int d\Omega' \ \sin\theta'\cos\phi' \int_0^a dr' \ r'^2 \ c(\vec{r}_i + \vec{r}', t) \tag{3.18}$$

$$p_{iy}(t) = \int d\Omega' \ \sin\theta'\sin\phi' \int_0^a dr' \ r'^2 \ c(\vec{r}_i + \vec{r}', t) \tag{3.19}$$

$$p_{iz}(t) = \int d\Omega' \ \cos\theta' \int_0^a dr' \ r'^2 \ c(\vec{r}_i + \vec{r}', t), \tag{3.20}$$

where $d\Omega' = \sin\theta'd\theta'd\phi'$. The r' coordinates are relative to the center of the respective cell, and the r_i coordinates are relative to the center of the collective. Using the mean concentration (Eq. 4.14) with a constant gradient $\vec{g} = g\hat{z}$, we calculate the mean polarization of a single cell:

$$\begin{aligned}
\langle p_{iz} \rangle &= \int d\Omega' \ \cos\theta' \int_0^a dr' \ r'^2 \ \bar{c}(\vec{r}_i + \vec{r}') \\
&= \int_0^a dr' \ r'^2 \int d\Omega' \ \cos\theta'(c_0 + gr_i\cos\theta_i + gr'\cos\theta') \\
&= \frac{\pi}{3}a^4 g \ .
\end{aligned}$$

The means for the x and y components are $\langle p_{ix} \rangle = \langle p_{iy} \rangle = 0$ since they are perpendicular to the gradient. On average, cells performing IC migration will only polarize in the z direction. The mean for a collective of IC cells is

$$\langle \vec{P} \rangle = \frac{\pi}{3}a^4 gN \ \hat{z} \ . \tag{3.21}$$

3.2.2 Emergent Chemotaxis

In EC, cells along the edge of the cluster polarize outwards, whereas cells in the interior are not involved in chemical sensing and remain unpolarized:

$$\vec{p}_i(t) = \begin{cases} \hat{r}_i \int_{U_i} d^3r \ c(\vec{r}, t) & i \in \{N_{\text{edge}}\} \\ 0 & i \in \{N_{\text{bulk}}\} \ , \end{cases} \tag{3.22}$$

where $\hat{r}$ points radially outwards from the collective. In order to break down $\vec{p}_i(\vec{r}, t)$ into component vectors we must be mindful of the dependence of $\hat{r}_i$ on the cell location. For an edge cell the unit vector $\hat{r}_i$ points in the direction of the cell's location in

the collective, $\hat{r}_i = \sin\Theta_i\cos\Phi_i\hat{x} + \sin\Theta_i\sin\Phi_i\hat{y} + \cos\Theta_i\hat{z}$ where Θ_i is the polar angle made with the gradient direction and Φ_i is the azimuthal angle along the collective. The cell component vectors are

$$p_{ix}(t) = \sin\Theta_i\cos\Phi_i \; p_i(t), \tag{3.23}$$

$$p_{iy}(t) = \sin\Theta_i\sin\Phi_i \; p_i(t) \;, \tag{3.24}$$

$$p_{iz}(t) = \cos\Theta_i \; p_i(t) \;, \tag{3.25}$$

with $p_i(t) = \int_{U_i} d^3r \; c(\vec{r}, t)$ and $i \in \{N_{\text{edge}}\}$. The total polarization of the collective, $\vec{P} = \vec{P}_x + \vec{P}_y + \vec{P}_z$, is a sum of all the component vectors:

$$P_x(t) = \sum_i^{N_{\text{edge}}} \sin\Theta_i\cos\Phi_i \; p_i(t) \;, \tag{3.26}$$

$$P_y(t) = \sum_i^{N_{\text{edge}}} \sin\Theta_i\cos\Phi_i \; p_i(t) \;, \tag{3.27}$$

$$P_z(t) = \sum_i^{N_{\text{edge}}} \cos\Theta_i \; p_i(t) \;. \tag{3.28}$$

For an edge cell, the mean polarization is equal to the average number of molecules the cell counts within its spherical body:

$$\begin{aligned}
\langle \vec{p}_i \rangle &= \int_{U_i} d^3r \; \bar{c}(\vec{r}) \; \hat{r}_i \\
&= \frac{4\pi}{3} a^3 (c_0 + gR\cos\Theta_i) \; \hat{r}_i \;,
\end{aligned}$$

where Θ_i is the angle the cell's location makes with the gradient direction. The mean for a cluster of EC cells will depend on the dimensionality of the cluster. For a 1D chain of cells, only the two cells on the opposite ends of the chain are polarized, and $\langle P \rangle$ is the difference in the mean number of molecules counted in between the two edge cells:

$$1\text{D} : \langle \vec{P} \rangle = \frac{8\pi}{3} a^4 g(N-1) \; \hat{z} \;. \tag{3.29}$$

In order to calculate the mean total polarization for two and three dimensional clusters we assume that the cluster size is relatively large ($a \ll R$) and approximate

the sum as an integral. For a 2D disc of cells the sum $\vec{P} = \sum_i^{N_{\text{edge}}} \vec{p}_i$ becomes an integral over the circumference of the cluster. The circumference and the total number of cells along the edge are related by $2\pi R = 2a N_{\text{edge}}$, and so a segment along the perimeter of length $R\theta$ is equivalent in length to $2an$ with n the number of edge cells in that segment. Hence $n = \frac{R}{2a}\theta$ allowing us to write integrals for $\vec{P}(t)$ as

$$\vec{P}(t) = \frac{R}{2a} \int_0^{2\pi} d\theta \; \vec{p}_i(t) \; . \tag{3.30}$$

The mean polarization will point only in the z direction with magnitude

$$\langle P_z \rangle = \frac{R}{2a} \int_0^{2\pi} d\theta \; \langle p_z \rangle = \frac{R}{2a} \int_0^{2\pi} d\theta \; \cos\theta \left(\frac{4\pi}{3} a^3 (c_0 + gR\cos\theta) \right) = \frac{2\pi^2}{3} a^2 g R^2 \; .$$

Using the relation $N = (R/a)^2$, the mean of the total polarization is

$$2\text{D} : \langle \vec{P} \rangle = \frac{2\pi^2}{3} a^4 g N \; \hat{z} \; . \tag{3.31}$$

Similarly, in 3D we approximate the sum as an integral of the spherical surface of the cluster. A patch on the surface of area ΩR^2 encompasses $n = \Omega R^2/(\pi a^2)$ edge cells. The total polarization can therefore be written as an integral over the surface of a spherical cluster:

$$\vec{P}(t) = \frac{R^2}{\pi a^2} \int d\Omega \; \vec{p}_i(t) \; . \tag{3.32}$$

The mean polarization will point only in the z direction with magnitude

$$\langle P_z \rangle = \frac{R^2}{\pi a^2} \int d\Omega \; \langle p_z \rangle = \frac{R^2}{\pi a^2} \int d\Omega \; \cos\theta \left(\frac{4\pi}{3} a^3 (c_0 + gR\cos\theta) \right) = \frac{16\pi}{9} a g R^3 \; .$$

For a spherical cluster, $N = (R/a)^3$ and the mean of the total cluster polarization is

$$3\text{D} : \langle \vec{P} \rangle = \frac{16\pi}{9} a^4 g N \; \hat{z} \; . \tag{3.33}$$

3.2.3 Variance in Cell & Cluster Polarization

Here we derive the variance in cell and collective polarizations. The first section gives a general outline for how this is done for either collective migration mechanism. The following sections will derive the specific expressions for IC, and EC and provide scaling arguments for 1D, 2D and 3D geometries.

General Outline

Since the total collective polarization is a sum of the cell polarization for IC or EC, the variance in the total polarization takes the general form:

$$\text{Var}[P_\alpha] = \underbrace{\sum_{i=1}^{N} \text{Var}[p_{i,\alpha}]}_{\text{variance contribution}} + \underbrace{\sum_{i \neq j} \text{Cov}[p_{i,\alpha}, p_{j,\alpha}]}_{\text{covariance contribution}} \tag{3.34}$$

$$\equiv V + C \ ,$$

with $\alpha \in \{x, y, z\}$. In order to derive an expression for the variance in collective polarization we must first understand the fluctuations occurring in single cell measurements. The fluctuations in the ith cell's polarization vector are calculated by linearizing each component, $p_{i,\alpha}(t) = \bar{p}_{i,\alpha} + \delta p_{i,\alpha}(t)$ and taking the Fourier transform. The Fourier transform of $\delta p_{i,\alpha}(t)$ takes the general form

$$\delta\tilde{p}_{i,\alpha}(\omega) = \int d^3 x_i \int \frac{d^3 k}{(2\pi)^3} f(\theta_i, \phi_i) \ \delta\tilde{c}(\vec{k}, \omega) \ e^{-i\vec{k}\cdot(\vec{x}_i + \vec{x})} \tag{3.35}$$

where the functional form of $f(\theta_i, \phi_i)$ is dictated by the migration mechanism (EC or IC) and the component α. The cross-spectrum between the ith and j^{th} cells is $\langle \delta\tilde{p}_{i,\alpha}^*(\omega') \delta\tilde{p}_{j,\alpha}(\omega) \rangle$. Utilizing the cross-spectrum we can derive an expression for the variance and covariance in the long-time averaged cell polarization by calculating the power spectrum

$$S_{ij,\alpha}(\omega = 0) = \lim_{\omega \to 0} \int \frac{d\omega'}{2\pi} \langle \delta\tilde{p}_{i,\alpha}^*(\omega') \delta\tilde{p}_{j,\alpha}(\omega) \rangle \ . \tag{3.36}$$

The cell polarization variance and covariance is given by:

$$\text{Var}[p_{i,\alpha}] = \frac{1}{T} S_{ii,\alpha}(0) \ , \tag{3.37}$$

$$\text{Cov}[p_{i,\alpha}, p_{j,\alpha}] = \frac{1}{T} S_{ij,\alpha}(0) \ , \tag{3.38}$$

where T is the averaging time. With the above expressions for the cell polarization variance and covariance we can solve for Eq. 4.34 and in turn calculate the relative error for the whole collective. In subsequent sections we show the derivation only for

the z component of the polarization since it is parallel to the gradient. The expressions x and y components will be equal to to the z component since the fluctuations in concentration are symmetric in each direction.

3.2.4   Individual-based Chemotaxis

For IC the variance in P_z is

$$\mathrm{Var}[P_z] = \sum_{i=1}^{N} \mathrm{Var}[p_{i,z}] + \sum_{i \neq j} \mathrm{Cov}[p_{i,z}, p_{j,z}] \equiv V_{\mathrm{IC}} + C_{\mathrm{IC}} . \tag{3.39}$$

The Fourier-transformed fluctuations in IC cell polarization is

$$\delta\tilde{p}_{j,z}(\vec{k}, \omega) = \int_V d^3x \int \frac{d^3k}{(2\pi)^3} \cos\theta \, \delta\tilde{c}(\vec{k}, \omega) e^{-i\vec{k}\cdot(\vec{x}_i + \vec{x})} . \tag{3.40}$$

The cross-spectrum for the z-component between two cells is

$$\langle \delta\tilde{p}_{i,z}^*(\omega') \delta\tilde{p}_{j,z}(\omega) \rangle = \int_V d^3x d^3x' \int \frac{d^3k d^3k'}{(2\pi)^6} \cos\theta \cos\theta' \langle \delta\tilde{c}^*(\vec{k}', \omega') \delta\tilde{c}(\vec{k}, \omega) \rangle e^{-i\vec{k}\cdot(\vec{x}_j + \vec{x})} e^{i\vec{k}'\cdot(\vec{x}_i + \vec{x}')} . \tag{3.41}$$

We can rewrite Eq. 4.41 by noting that only the relative locations of cell i and j are relevant for the cross-spectrum. Let $\vec{r}_{ij} = \vec{x}_i - \vec{x}_j$ and $r_{ij} = |\vec{r}_{ij}|$.

$$\begin{aligned}
\langle \delta\tilde{p}_{i,z}^*(\omega') \delta\tilde{p}_{j,z}(\omega) \rangle = \int_V d^3x d^3x' \int \frac{d^3k d^3k'}{(2\pi)^6} \cos\theta \cos\theta' \\
\langle \delta\tilde{c}^*(\vec{k}', \omega') \delta\tilde{c}(\vec{k}, \omega) \rangle e^{-i\vec{k}\cdot\vec{x}} e^{i\vec{k}'\cdot(\vec{r}_{ij} + \vec{x}')}
\end{aligned} \tag{3.42}$$

Plugging in Eq. 4.16 for $\langle \delta\tilde{c}^*(\vec{k}', \omega') \delta\tilde{c}(\vec{k}, \omega) \rangle$ and writing $\cos\theta$ in terms of spherical harmonic $Y_1^0(\hat{x})$ yields

$$\begin{aligned}
\langle \delta\tilde{p}_{i,z}^*(\omega') \delta\tilde{p}_{j,z}(\omega) \rangle &= \int_V d^3x d^3x' \int \frac{d^3k d^3k'}{(2\pi)^6} \frac{4\pi}{3} Y_1^0(\hat{x}) Y_1^0(\hat{x}') \, 2D \\
&\quad \frac{2\pi\delta(\omega - \omega')}{(Dk^2 - i\omega)(Dk'^2 + i\omega')} \int d^3y \vec{k} \cdot \vec{k}' \bar{c}(\vec{y}) e^{i\vec{y}\cdot(\vec{k} - \vec{k}')} e^{-i\vec{k}\cdot\vec{x}} e^{i\vec{k}'\cdot(\vec{r}_{ij} + \vec{x}')} \\
&= \frac{4D}{3(2\pi)^5} 2\pi\delta(\omega - \omega') \int_V d^3x d^3x' \int d^3k d^3k' d^3y \, Y_1^0(\hat{x}) Y_1^0(\hat{x}') \\
&\quad \frac{\bar{c}(\vec{y}) \, \vec{k} \cdot \vec{k}' \, e^{i\vec{y}\cdot(\vec{k} - \vec{k}')}}{(Dk^2 - i\omega)(Dk'^2 + i\omega')} e^{-i\vec{k}\cdot\vec{x}} e^{i\vec{k}'\cdot(\vec{r}_{ij} + \vec{x}')}
\end{aligned}$$

Plugging in the above expression for $\langle \delta \tilde{p}^*_{i,z}(\omega') \delta \tilde{p}_{j,z}(\omega) \rangle$ into $S_{ij,z}(0)$ (Eq. 4.36) and using the specified mean concentration from Eq. 4.14:

$$S_{ij,z}(0) = \frac{4}{3(2\pi)^5 D} \int_V d^3x d^3x' \int d^3k d^3k' d^3y \; Y_1^0(\hat{x}) Y_1^0(\hat{x}') \frac{\vec{k} \cdot \vec{k}'}{k^2 k'^2}$$
$$(c_0 + \vec{g} \cdot \vec{y}) \; e^{i\vec{y}(\vec{k}-\vec{k}')} \; e^{-i\vec{k}\cdot\vec{x}} e^{i\vec{k}'\cdot(\vec{r}_{ij}+\vec{x}')} \; . \tag{3.43}$$

We can break up the expression for $S_{ij,z}(0)$ into two terms: one dependent on the background concentration, the other on the gradient.

$$S_{ij,z}(0) = \frac{4}{3(2\pi)^5 D} \int_V d^3x d^3x' \int d^3k d^3k' \; Y_1^0(\hat{x}) Y_1^0(\hat{x}') \frac{\vec{k} \cdot \vec{k}'}{k^2 k'^2} \; e^{-i\vec{k}\cdot\vec{x}}$$
$$e^{i\vec{k}'\cdot(\vec{r}_{ij}+\vec{x}')} \left((2\pi)^3 \delta^3(\vec{k}-\vec{k}') c_0 + \int d^3y \; \vec{g} \cdot \vec{y} \; e^{i\vec{y}(\vec{k}-\vec{k}')} \right) \tag{3.44}$$

Let S^1_{ij} represent the background concentration term and S^2_{ij} represent the gradient dependent term in the power spectrum such that $S_{ij,z}(0) = S^1_{ij} + S^2_{ij}$.

$$S^1_{ij} = \frac{4c_0}{3(2\pi)^2 D} \int_V d^3x d^3x' \int d^3k \; Y_1^0(\hat{x}) Y_1^0(\hat{x}') \frac{1}{k^2} \; e^{-i\vec{k}\cdot\vec{x}} \; e^{i\vec{k}\cdot(\vec{r}_{ij}+\vec{x}')} \tag{3.45}$$

$$S^2_{ij} = \frac{4c_0}{3(2\pi)^5 D} \int_V d^3x d^3x' \int d^3k d^3k' d^3y \; Y_1^0(\hat{x}) Y_1^0(\hat{x}') \frac{\vec{k} \cdot \vec{k}'}{k^2 k'^2} \; \vec{g} \cdot \vec{y}$$
$$e^{i\vec{y}(\vec{k}-\vec{k}')} \; e^{-i\vec{k}\cdot\vec{x}} \; e^{i\vec{k}'\cdot(\vec{r}_{ij}+\vec{x}')} \tag{3.46}$$

The following expansions will prove useful:

$$e^{-i\vec{k}\cdot\vec{r}} = 4\pi \sum_{l,m} (-i)^l j_l(kr) Y_l^m(\hat{k}) Y_l^{m*}(\hat{r}) \; , \tag{3.47}$$

$$\vec{a} \cdot \vec{b} = \frac{4\pi}{3} ab \sum_{m=-1}^{1} Y_1^m(\hat{a}) Y_1^{m*}(\hat{b}) \; . \tag{3.48}$$

Starting with Eq. 4.45 we expand all the exponential terms, and we use these expansions in order to evaluate the angular integrals in S^1_{ij}.

$$S^1_{ij} = \frac{2^5(2\pi)c_0}{3D} \int_V d^3x d^3x' \int d^3k \; Y_1^{0*}(\hat{x}) Y_1^{0*}(\hat{x}') \; \frac{1}{k^2}$$
$$\left(\sum_{l_1,m_1} i^{-l_1} j_{l_1}(xk) Y_{l_1}^{m_1}(\hat{x}) Y_{l_1}^{m_1*}(\hat{k}) \right) \left(\sum_{l_2,m_2} i^{l_2} j_{l_2}(r_{ij}k) Y_{l_2}^{m_2}(\hat{k}) Y_{l_2}^{m_2*}(\hat{r}_{ij}) \right) \tag{3.49}$$
$$\left(\sum_{l_3,m_3} i^{l_3} j_{l_3}(x'k) Y_{l_3}^{m_3}(\hat{k}) Y_{l_3}^{m_3*}(\hat{x}') \right)$$

The angular integrals over $\hat{x}$ and $\hat{x}'$ eliminate the summations over l_1, m_1 and l_3, m_3.

$$S_{ij}^1 = \frac{2^5(2\pi)c_0}{3D} \int_0^a dxdx' \int d^3k \frac{1}{k^2} x^2 x'^2 \, j_1(xk)j_1(x'k) \, Y_1^{0*}(\hat{k})Y_1^0(\hat{k})$$
$$\left(\sum_{l_2,m_2} i^{l_2} j_{l_2}(r_{ij}k') Y_{l_2}^{m_2}(\hat{k}')Y_{l_2}^{m_2*}(\hat{r}_{ij}) \right) \tag{3.50}$$

The product of the two spherical harmonics is

$$Y_1^{0*}(\hat{k})Y_1^{0*}(\hat{k}) = \frac{1}{\sqrt{4\pi}} \left(Y_0^0(\hat{k}) + \frac{2\sqrt{5}}{5} Y_2^0(\hat{k}) \right) \ .$$

Therefore when evaluating the $\hat{k}$ integral in Eq. 4.50 only the $l_2 = 0, m_2 = 0$ and $l_2 = 2, m_2 = 0$ terms of the summation will be non-zero.

$$S_{ij}^1 = \frac{2^5(2\pi)c_0}{3D\sqrt{4\pi}} \int_0^a dxdx' \int_0^\infty dk \, x^2 x'^2 \, j_1(xk)j_1(x'k)$$
$$\left(j_0(r_{ij}k)Y_0^0(\hat{r}_{ij}) - \frac{2\sqrt{5}}{5} j_2(r_{ij}k)Y_2^0(\hat{r}_{ij}) \right) \tag{3.51}$$

The integrals over x and x' evaluate to:

$$\int_0^a dx \, x^2 j_1(kx) = \frac{1}{k^3} \left(2 - 2\cos(ak) - ak\sin(ak) \right) \equiv \frac{1}{k^3} h(ak) \ .$$

Note that $Y_0^0(\Theta_{ij}, \Phi_{ij}) = \frac{1}{\sqrt{4\pi}}$, and $Y_2^0(\Theta_{ij}, \Phi_{ij}) = \frac{1}{2}\sqrt{\frac{5}{4\pi}}(3\cos^2\Theta_{ij} - 1)$. The angle Θ_{ij} is the angle $\hat{r}_{ij}$ makes relative to the gradient direction $\hat{g}$, $\cos\Theta_{ij} = \hat{r}_{ij} \cdot \hat{g}$. The expression for S_{ij}^1 reduces to

$$S_{ij}^1 = \frac{2^4 c_0}{3D} \int_0^\infty dk \, \frac{h^2(ak)}{k^6} \left[j_0(r_{ij}k) - j_2(r_{ij}k)(3\cos^2\Theta_{ij} - 1) \right] \tag{3.52}$$

We can make the integral dimensionless by making the variable substitutions $u \equiv ak$ and $n_{ij} \equiv r_{ij}/a$.

$$S_{ij}^1 = \frac{2^4 c_0 a^5}{3D} \int_0^\infty du \, \frac{h^2(u)}{u^6} \left[j_0(n_{ij}u) - j_2(n_{ij}u)(3\cos^2\Theta_{ij} - 1) \right] \tag{3.53}$$

We can break up Eq. 4.53 into two integrals and evaluate them individually. Note that the exact solution to either integral depends parametrically on n_{ij} and that n_{ij} is the number of cells radii separating two cells. If we are evaluating the cross-correlations

in one cell then $i = j$ and $n_{ii} = 0$; on the other hand, if $i \neq j$ then $n_{ij} \geq 2$ in order to eliminate the possibility of overlapping cells. In either case the expression simplifies to:

$$S_{ij}^1 = \begin{cases} \frac{4\pi c_0 a^5}{45D} & i = j \\ -\frac{\pi c_0 a^5}{18D} \frac{1}{n_{ij}^3} (3\cos^2 \Theta_{ij} - 1) & i \neq j, \ n_{ij} \geq 2 \end{cases} . \tag{3.54}$$

Doing the same set of expansions for S_{ij}^2 in Eq. 4.46, and performing the same kind of analysis reveals that the gradient depedendent term is asymmetric under exchange of i and j. Therefore when calculating the cluster polarization variance all the S_{ij}^2 terms will cancel. The variance contributions V and C are

$$V_{\text{IC}} = \sum_{i=1}^{N} \frac{1}{T} S_{ii,z}(0) = \frac{4\pi a^5 c_0}{45DT} N \ , \tag{3.55}$$

$$C_{\text{IC}} = \sum_{i\neq j}^{N} \frac{1}{T} S_{ij,z}(0) = -\frac{\pi a^5 c_0}{18DT} \sum_{i\neq j}^{N} \frac{(3\cos^2 \Theta_{ij} - 1)}{n_{ij}^3} \ , \tag{3.56}$$

resulting in the IC collective total variance

$$\text{Var}[P_z] = \frac{\pi a^5 c_0}{9DT} \left[\frac{4}{5} N - \frac{1}{2} \sum_{i\neq j}^{N} \frac{(3\cos^2 \Theta_{ij} - 1)}{n_{ij}^3} \right] \ , \tag{3.57}$$

as in Eqs. 6 and 7 in the main text. Next we will show how Eq. 4.57 scales for collectives in one, two and three dimensional configurations.

One Dimensional Chain

For a one-dimensional chain of IC cells each cell is aligned parallel to the gradient and the angular dependence of C_{IC} (Eq. 4.56) vanishes,

$$C_{\text{IC}} = -\frac{\pi a^5 c_0}{18DT} \sum_{i\neq j}^{N} \frac{2}{n_{ij}^3} \ . \tag{3.58}$$

We evaluate the sum:

$$\sum_{i\neq j}^{N} \frac{1}{n_{ij}^3} = 2 \sum_{i<j}^{N} \frac{1}{n_{ij}^3} = 2 \sum_{i=1}^{N-1} \frac{N-i}{(2i)^3} = \frac{1}{4}(NH_{N-1}^{(3)} - H_{N-1}^{(2)}) \ ,$$

with $H_n^{(m)} = \sum_{k=1}^{n} \frac{1}{k^m}$ the generalized harmonic number. This results in a total variance of the form

$$\text{Var}[P_z] = \frac{\pi a^5 c_c}{9DT}\left[\frac{4}{5}N - \frac{1}{8}\left(NH_{N-1}^{(3)} - H_{N-1}^{(2)}\right)\right] . \tag{3.59}$$

For large N, $H_{N-1}^{(i)}$ approaches a constant for $i \geq 2$. Therefore, we see that $\text{Var}[P_z]$ scales with N for 1D IC collectives as in Table I of the main text.

Two Dimensional Sheet

For a two-dimensional sheet of IC cells, pairs of cells can now make a variety of angles with the gradient, and the angular dependence of C_{IC} cannot be easily simplified. In order to find the N scaling for C_{IC} we calculate the sum numerically. Since the covariances rapidly fall-off as $1/n_{ij}^3$, we only track nearest neighbor pairs that are less than 3 cell radii apart. The resulting numerical solution to the sum in C_{IC} is

$$\sum_{i \neq j}^{N} \frac{3\cos^2\Theta_{ij} - 1}{n_{ij}^3} = 2\sum_{i < j}^{N} \frac{3\cos^2\Theta_{ij} - 1}{n_{ij}^3} = \frac{1}{4}(1.70N - 2.67\sqrt{N} + 0.89) .$$

Therefore the expression for C_{IC} (Eq. 4.56) simplifies to

$$C_{\text{IC}} = -\frac{\pi a^5 c_0}{18DT}(0.43N - 0.67\sqrt{N} + 0.22) . \tag{3.60}$$

The covariance contribution, C_{IC}, to leading order scales linearly with N. The total variance becomes

$$\text{Var}[P_z] = \frac{\pi a^5 c_c}{9DT}\left(0.59N + 0.33\sqrt{N} - 0.11\right) . \tag{3.61}$$

We see that for large N, $\text{Var}[P_z]$ scales with N for 2D IC collectives as in Table I in the main text.

Three Dimensional Cluster

To obtain a scaling for C_{IC} in a three dimensional cluster we assume that cluster is large, such that $a \ll R$ and $N \gg 1$. For a given cell we can calculate its contribution

to C_{IC} by considering the covariance contribution it makes with a set of cells a fixed distance away from it. The equidistant cells form a spherical shell with the principal cell in the center. Adapting Eq. 4.56 for a cell and its spherical shell of covariance pairs yields:

$$C_{\mathrm{cell}} = -\frac{\pi a^5 c_0}{18DT} \frac{1}{n_{\mathrm{shell}}^3} \sum_{i_{\mathrm{shell}}} 3 \cos^2 \Theta_i - 1 , \qquad (3.62)$$

with n_{shell} the radius of the shell in terms of cell radii. Going to continuum we can calculate the contribution from the cell and all its pairs

$$C_{\mathrm{cell}} = -\frac{\pi a^5 c_0}{18DT n_{\mathrm{shell}}^3} \int_0^{2\pi} d\phi \int_0^{\pi} d\theta \, \sin\theta (3\cos^2\theta - 1) = -\frac{\pi^2 a^5 c_0}{9DT n_{\mathrm{shell}}^3} \int_0^{\pi} d\theta \, (3\cos^2\sin\theta - \sin\theta) = 0 . \tag{3.63}$$

In the last step, we see that the integral vanishes. Thus, the contribution from a single cell and its shell of pairs sum to zero. Repeating this argument for all cells in the cluster results in the total $C_{\mathrm{IC}} = 0$. Therefore for 3D clusters there is no covariance contribution to the total variance, and $\mathrm{Var}[P_z] = V_{\mathrm{IC}} \sim N$ as in Table I of the main text.

3.2.5 Emergent Chemotaxis Clusters

For EC the variance in P_z is

$$\mathrm{Var}[P_z] = \sum_{i=1}^{N} \mathrm{Var}[p_{i,z}] + \sum_{i \neq j} \mathrm{Cov}[p_{i,z}, p_{j,z}] \equiv V_{\mathrm{EC}} + C_{\mathrm{EC}} . \tag{3.64}$$

The Fourier-transformed fluctuations in IC cell polarization is

$$\delta \tilde{p}_{i,z}(\vec{k}, \omega) = \cos\Theta_i \int_V d^3x \int \frac{d^3k}{(2\pi)^3} \delta\tilde{c}(\vec{k}, \omega) e^{-i\vec{k}\cdot(\vec{x}_i + \vec{x})} , \tag{3.65}$$

with Θ_i the angle cell i makes with the gradient. The cross-spectrum for the z-component between two cells is

$$\langle \delta\tilde{p}_i^*(\vec{k'}, \omega') \delta\tilde{p}_j(\vec{k}, \omega) \rangle = \cos\Theta_i \cos\Theta_j \int_V d^3x d^3x' \int \frac{d^3k d^3k'}{(2\pi)^6} \langle \delta\tilde{c}^*(\vec{k'}, \omega') \delta\tilde{c}(\vec{k}, \omega) \rangle e^{-i\vec{k}\cdot(\vec{x}_j + \vec{x})} e^{i\vec{k}\cdot(\vec{x}_i + \vec{x}')} \tag{3.66}$$

Following the same procedure as in the case of IC, we get an expression for S_{ij}^1 for EC:

$$S_{ij}^1 = \begin{cases} \frac{16\pi c_0 a^5}{15D} \cos^2 \Theta_i & i = j \\ \frac{8\pi c_0 a^5}{9D} \frac{1}{n_{ij}} \cos \Theta_i \cos \Theta_j & i \neq j, \ n_{ij} \geq 2 \end{cases} . \tag{3.67}$$

Since again $S_{ij}^2 = 0$ by symmetry, the variance for any configuration of EC cells is

$$V_{\text{EC}} = \frac{16\pi a^5 c_0}{15DT} \sum_{i=1}^{N_{\text{edge}}} \cos^2 \Theta_i \ , \tag{3.68}$$

$$C_{\text{EC}} = \frac{8\pi a^5 c_0}{9DT} \sum_{i \neq j} \frac{\cos \Theta_i \cos \Theta_j}{n_{ij}} \ , \tag{3.69}$$

as in Eqs. 10 and 11 in the main text. The resulting total variance is

$$\text{Var}[P_z] = \frac{8\pi a^5 c_0}{3DT} \left[\frac{2}{5} \sum_{i=1}^{N_{\text{edge}}} \cos^2 \Theta_i + \frac{1}{3} \sum_{i \neq j} \frac{\cos \Theta_i \cos \Theta_j}{n_{ij}} \right] . \tag{3.70}$$

One Dimensional Chain

For a one-dimensional chain of cells only the two cells on the opposing ends are polarized. The cell variance contribution to the total variance therefore does not change with increasing cluster size,

$$V_{\text{EC}} = \frac{16\pi a^5 c_0}{15DT} \sum_{i=1}^{N_{\text{edge}}} \cos^2 \Theta_i = \frac{32\pi a^5 c_0}{15DT} \ . \tag{3.71}$$

Therefore $V_{\text{EC}} \sim N^0$ for 1D collectives. For C_{EC} the distance between the two edge cells increases by two cell radii for each cell added to the chain:

$$C_{\text{EC}} = \frac{8\pi a^5 c_0}{9DT} \sum_{i \neq j} \frac{\cos \Theta_i \cos \Theta_j}{n_{ij}} = -\frac{8\pi a^5 c_0}{9DT} \frac{1}{2(N-1)} \ . \tag{3.72}$$

So $C_{\text{EC}} \sim N^{-1}$ for 1D collectives. To leading order in N the total collective variance depends only on V_{EC}:

$$\text{Var}[P_z] = \frac{32\pi a^5 c_0}{15DT} \ , \tag{3.73}$$

and so $\text{Var}[P_z]$ does not depend on collective size for 1D EC as in Table I of the main text.

Two Dimensional Sheet

In order to evaluate the variance for a two-dimensional disc of cells we will approximate the sums as integrals over the circumference of the disc as we did in evaluating the mean polarization. Assuming that $a \ll R$ Eq. 4.68 can be written as an integral

$$V_{\mathrm{EC}} = \frac{16\pi a^5 c_0}{15DT} \frac{R}{2a} \int_0^{2\pi} d\theta \ \cos^2 \theta \ . \tag{3.74}$$

Using the relation $N = (R/a)^2$ yields

$$V_{\mathrm{EC}} = \frac{8\pi^2 a^5 c_0}{15DT} \sqrt{N} \ . \tag{3.75}$$

Hence for 2D EC, the variance contribution V_{EC} scales as $\sqrt{N}$. In order to determine how C_{EC} scales with N we approximate the sums over i and j as a double integral, again assuming that $a \ll R$.

$$C_{\mathrm{EC}} = \frac{16\pi a^5 c_0}{9DT} \left(\frac{R}{2a^2} \right) \int_{\Delta/2}^{2\pi - \Delta/2} d\theta_1 \int_{\theta_1 + \Delta/2}^{2\pi} d\theta_2 \ \frac{\cos\theta_1 \cos\theta_2}{n(\theta_1, \theta_2)} \tag{3.76}$$

Here $\Delta = 2a/R$ is the anguler separation between two edge cells, and

$$n(\theta_1, \theta_2) = \frac{2R}{a} \sin\left(\frac{1}{2}(\theta_2 - \theta_1) \right)$$

is the number of cell radii separating two edge cells. Using this expression for $n(\theta_1, \theta_2)$ we evaluate the integral over θ_2:

$$\left(\frac{R}{2a^2} \right) \int_{\Delta/2}^{2\pi - \Delta/2} d\theta_1 \int_{\theta_1 + \Delta/2}^{2\pi} d\theta_2 \ \frac{\cos\theta_1 \cos\theta_2}{n(\theta_1, \theta_2)}$$

$$= \frac{R}{8a} \int_{\Delta/2}^{2\pi - \Delta/2} d\theta_1 \cos\theta_1 [-4 \left(\cos(\theta_1/2) + \cos(\theta_1 + \Delta/2) \right) - 2\cos\theta_1 \log\left(\tan(\Delta/4) \tan \right.$$

$$\tag{3.77}$$

Breaking up the integral into four separate terms we find:

$$\int_{\Delta/2}^{2\pi - \Delta/2} d\theta_1 \cos\theta_1 \cos(\theta_1/2) = 0 \ ,$$

$$\int_{\Delta/2}^{2\pi - \Delta/2} d\theta_1 \cos\theta_1 \cos(\theta_1 + \Delta/2) = -\frac{1}{2} \cos(\Delta/2)(\Delta + \sin\Delta - 2\pi) \ ,$$

$$\int_{\Delta/2}^{2\pi - \Delta/2} d\theta_1 \cos\theta_1 \log\left(\tan(\Delta/4) \right) = -\frac{1}{2}(\Delta + \sin\Delta - 2\pi) \tan(\Delta/4) \ ,$$

$$\int_{\Delta/2}^{2\pi - \Delta/2} d\theta_1 \cos\theta_1 \log\left(\tan(\theta_1/4) \right) = 0 \ .$$

The first and last integrals are equal to zero since the integrands are odd functions over the range $[0, 2\pi]$. With these results, the whole expression simplifies to

$$C_{\text{EC}} = \frac{16\pi a^5 c_0}{9DT} \frac{1}{4} \sqrt{N} \left(\frac{1}{2} \log N + \log 2 - 2 \right) \left(\pi - \frac{2}{\sqrt{N}} \right) \qquad (3.78)$$

Keeping only the leading order terms in N yields

$$C_{\text{EC}} = \frac{2\pi a^5 c_0}{9DT} \sqrt{N} \log N . \qquad (3.79)$$

The resulting total variance is

$$\text{Var}[P_z] = \frac{8\pi a^5 c_0}{3DT} \sqrt{N} \left[\frac{\pi}{5} + \frac{1}{12} \log N \right] , \qquad (3.80)$$

which to to leading order scales as $\sqrt{N} \log N$ as in Table I of the main text.

Three Dimensional Cluster

For the three-dimensional cluster, numerical methods must be used in order to find the scaling properties of the variance. We numerically evaluate the total variance (Eq. 4.70) on a cubic lattice and obtain the following results.
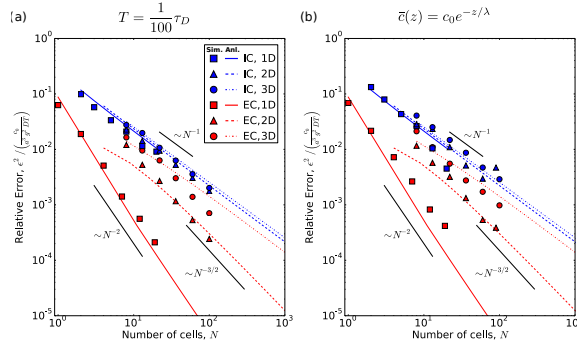

Fig. 3.3. $\text{Var}[P_z]$ for a 3D cluster of EC cells. Cluster variance shown in red. Pink circles are the single cell variance contributions V, and pink diamonds are the cell-cell covariance contributions C.

The numerical results [Fig. 4.3] show that $V \sim N^{2/3}$ since the number of edge cells also scales as $N^{2/3}$. We also find that $C \sim N$; the covariance contribution to

the total cluster polarization grows linearly with N. For large clusters the N scaling dominates the behavior of $\mathrm{Var}[P_z]$. Therefore, in 3D the leading order scaling for the variance is $\mathrm{Var}[P_z] \sim N$ as in Table I of the main text.
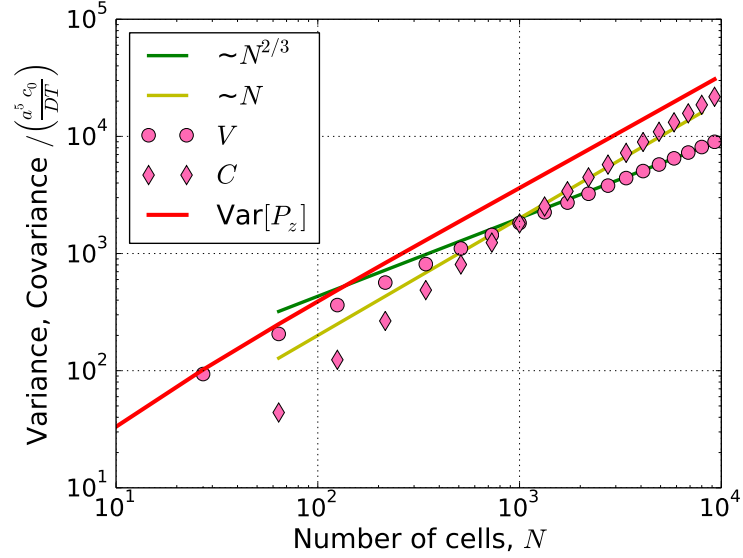
3.3   Testing Analytic Model Assumptions

Fig. 3.4. (a) Short-time integration relative error results. Data points are of simulations for $T = \frac{1}{100}\tau_D$. (b) Exponential concentration profile relative error results. The mean concentration profile is $\bar{c}(z) = c_0 e^{-z/\lambda}$, the lengthscale $\lambda = \sqrt{D/\beta}$ is set by the diffusion coefficient D and the molecule decay rate β. Lines are from original analytical predictions using $T > \tau_D$ and a linear concentration profile.

Simulations are performed to test model behavior when assumptions used to derive analytic results are relaxed. In Fig. 4.4(a) we relax the assumption that the integration time T must be larger than the timescale for diffusion $\tau_D \sim R^2/D$. We find that ϵ^2 scales the same way as previously predicted for both EC and IC, even when $T = \tau_D/100$. The only exception is that ϵ^2 for 3D EC [Fig. 4.4(a), red circles] has a more negative power-law dependence on N than the expected $\sim N^{-1}$. The

shorter integration time results in decreased correlations between edge cells which when $T > \tau_D$ results in $C \sim N$. Hence with $T < \tau_D$ the total variance is less dependent on C, and $V \sim N^{2/3}$ becomes the dominant contribution to $\mathrm{Var}[P]$. This results in a steeper scaling of ϵ^2 closer to $\mathrm{Var}[P]/\langle P \rangle^2 \sim N^{2/3}/N^2 = N^{-4/3}$. Interestingly, we see that relaxing the assumption $T \gg \tau_D$ results in improved precision for EC over IC not just in 1D and 2D but also in 3D configurations.

In Fig. 4.4(b) we change the concentration profile from linear to exponential which has a mean concentration of $\bar{c}(z) = c_0 e^{-z/\lambda}$. The lengthscale $\lambda = \sqrt{D/\beta}$ depends on the diffusion coefficient and the molecule degradation rate β. In Fig. 4.4(b) the simulation results are for $\lambda > a$. We find that ϵ^2 is in very good agreement with our original analytic predictions. The only exception is that due to the exponential profile, $\langle P \rangle$ for 1D EC (Fig. 4.4(b), red squares) is non-linear in N causing the relative error data to scale less steeply than the expected N^{-2}.

REFERENCES

REFERENCES

[1] L. Song, S. M. Nadkarni, H. U. Bödeker, C. Beta, A. Bae, C. Franck, W.-J. Rappel, W. F. Loomis, and E. Bodenschatz, "Dictyostelium discoideum chemotaxis: threshold for directed motion," *European journal of cell biology*, vol. 85, no. 9, pp. 981–989, 2006.

[2] H. C. Berg and E. M. Purcell, "Physics of chemoreception." *Biophysical journal*, vol. 20, no. 2, p. 193, 1977.

[3] W. Bialek and S. Setayeshgar, "Physical limits to biochemical signaling," *Proceedings of the National Academy of Sciences of the United States of America*, vol. 102, no. 29, pp. 10 040–10 045, 2005.

[4] K. Kaizu, W. de Ronde, J. Paijmans, K. Takahashi, F. Tostevin, and P. R. ten Wolde, "The berg-purcell limit revisited," *Biophysical journal*, vol. 106, no. 4, pp. 976–985, 2014.

[5] B. A. Bicknell, P. Dayan, and G. J. Goodhill, "The limits of chemosensation vary across dimensions," *Nature communications*, vol. 6, 2015.

[6] D. Ellison, A. Mugler, M. D. Brennan, S. H. Lee, R. J. Huebner, E. R. Shamir, L. A. Woo, J. Kim, P. Amar, I. Nemenman *et al.*, "Cell–cell communication enhances the capacity of cell ensembles to sense shallow gradients during morphogenesis," *Proceedings of the National Academy of Sciences*, p. 201516503, 2016.

[7] W. J. Rosoff, J. S. Urbach, M. A. Esrick, R. G. McAllister, L. J. Richards, and G. J. Goodhill, "A new chemotaxis assay shows the extreme sensitivity of axons to molecular gradients," *Nature neuroscience*, vol. 7, no. 6, pp. 678–682, 2004.

[8] A. Mugler, A. Levchenko, and I. Nemenman, "Limits to the precision of gradient sensing with spatial communication and temporal integration," *Proceedings of the National Academy of Sciences*, p. 201509597, 2016.

[9] A. Levchenko and P. A. Iglesias, "Models of eukaryotic gradient sensing: application to chemotaxis of amoebae and neutrophils," *Biophysical journal*, vol. 82, no. 1, pp. 50–63, 2002.

[10] P. Friedl and K. Wolf, "Plasticity of cell migration: a multiscale tuning model," *The Journal of cell biology*, vol. 188, no. 1, pp. 11–19, 2010.

[11] T. B. Rasmussen and M. Givskov, "Quorum-sensing inhibitors as anti-pathogenic drugs," *International Journal of Medical Microbiology*, vol. 296, no. 2, pp. 149–161, 2006.

[12] M. C. Boelens, T. J. Wu, B. Y. Nabet, B. Xu, Y. Qiu, T. Yoon, D. J. Azzam, C. Twyman-Saint Victor, B. Z. Wiemann, H. Ishwaran, P. J. ter Brugge, J. Jonkers, J. Slingerland, and A. J. Minn, "Exosome transfer from stromal to breast cancer cells regulates therapy resistance pathways," *Cell*, vol. 159, no. 3, pp. 499–513, 2014.

[13] K. J. Cheung, E. Gabrielson, Z. Werb, and A. J. Ewald, "Collective invasion in breast cancer requires a conserved basal epithelial program," *Cell*, vol. 155, no. 7, pp. 1639–1651, 2013.

[14] P. Vader, X. O. Breakefield, and M. J. Wood, "Extracellular vesicles: emerging targets for cancer therapy," *Trends in molecular medicine*, vol. 20, no. 7, pp. 385–393, 2014.

[15] A. J. Kabla, "Collective cell migration: leadership, invasion and segregation," *Journal of The Royal Society Interface*, p. rsif20120448, 2012.

[16] A. Szabó, R. Ünnep, E. Méhes, W. Twal, W. Argraves, Y. Cao, and A. Czirók, "Collective cell motion in endothelial monolayers," *Physical biology*, vol. 7, no. 4, p. 046007, 2010.

[17] M. Basan, J. Elgeti, E. Hannezo, W.-J. Rappel, and H. Levine, "Alignment of cellular motility forces with tissue flow as a mechanism for efficient wound healing," *Proceedings of the National Academy of Sciences*, vol. 110, no. 7, pp. 2452–2459, 2013.

[18] A. Janulevicius, M. van Loosdrecht, and C. Picioreanu, "Short-range guiding can result in the formation of circular aggregates in myxobacteria populations," *PLoS Comput Biol*, vol. 11, 2015.

[19] P. Friedl, J. Locker, E. Sahai, and J. E. Segall, "Classifying collective cancer cell invasion," *Nature Cell Biology*, vol. 14, no. 8, pp. 777–783, 2012.

[20] J. D. Shields, M. E. Fleury, C. Yong, A. A. Tomei, G. J. Randolph, and M. A. Swartz, "Autologous chemotaxis as a mechanism of tumor cell homing to lymphatics via interstitial flow and autocrine ccr7 signaling," *Cancer cell*, vol. 11, no. 6, pp. 526–538, 2007.

[21] M. F. Leber and T. Efferth, "Molecular principles of cancer invasion and metastasis (review)," *International journal of oncology*, vol. 34, no. 4, pp. 881–895, 2009.

[22] D. Hanahan and R. A. Weinberg, "The hallmarks of cancer," *cell*, vol. 100, no. 1, pp. 57–70, 2000.

[23] ——, "Hallmarks of cancer: the next generation," *cell*, vol. 144, no. 5, pp. 646–674, 2011.

[24] N. A. Bhowmick, E. G. Neilson, and H. L. Moses, "Stromal fibroblasts in cancer initiation and progression," *Nature*, vol. 432, no. 7015, pp. 332–337, 2004.

[25] J. Condeelis and J. W. Pollard, "Macrophages: obligate partners for tumor cell migration, invasion, and metastasis," *Cell*, vol. 124, no. 2, pp. 263–266, 2006.

[26] A. Puliafito, A. De Simone, G. Seano, P. A. Gagliardi, L. Di Blasio, F. Chianale, A. Gamba, L. Primo, and A. Celani, "Three-dimensional chemotaxis-driven aggregation of tumor cells," *Scientific reports*, vol. 5, 2015.

[27] W. J. Polacheck, J. L. Charest, and R. D. Kamm, "Interstitial flow influences direction of tumor cell migration through competing mechanisms," *Proceedings of the National Academy of Sciences*, vol. 108, no. 27, pp. 11 115–11 120, 2011.

[28] A. C. Shieh and M. A. Swartz, "Regulation of tumor invasion by interstitial fluid flow," *Physical biology*, vol. 8, no. 1, p. 015012, 2011.

[29] N. Aceto, A. Bardia, D. T. Miyamoto, M. C. Donaldson, B. S. Wittner, J. A. Spencer, M. Yu, A. Pely, A. Engstrom, H. Zhu, B. W. Brannigan, R. Kapur, S. L. Stott, T. Shioda, S. Ramaswamy, D. T. Ting, C. P. Lin, M. Toner, D. A. Haber, and S. Maheswaran, "Circulating tumor cell clusters are oligoclonal precursors of breast cancer metastasis," *Cell*, vol. 158, no. 5, pp. 1110–1122, 2014.

[30] F. Dahlquist, R. Elwell, and P. S. Lovely, "Studies of bacterial chemotaxis in defined concentration gradients. a model for chemotaxis toward l-serine," *Journal of supramolecular structure*, vol. 4, no. 3, pp. 329–342, 1976.

[31] A. Jilkine and L. Edelstein-Keshet, "A comparison of mathematical models for polarization of single eukaryotic cells in response to guided cues," *PLoS Comput Biol*, vol. 7, no. 4, pp. e1 001 121–e1 001 121, 2011.

[32] R. G. Endres and N. S. Wingreen, "Accuracy of direct gradient sensing by cell-surface receptors," *Progress in biophysics and molecular biology*, vol. 100, no. 1, pp. 33–39, 2009.

[33] B. Hu, W. Chen, W.-J. Rappel, and H. Levine, "Physical limits on cellular sensing of spatial gradients," *Physical review letters*, vol. 105, no. 4, p. 048104, 2010.

[34] R. G. Endres and N. S. Wingreen, "Accuracy of direct gradient sensing by single cells," *Proceedings of the National Academy of Sciences*, vol. 105, no. 41, pp. 15 749–15 754, 2008.

[35] P. J. Van Haastert and M. Postma, "Biased random walk by stochastic fluctuations of chemoattractant-receptor interactions at the lower limit of detection," *Biophysical journal*, vol. 93, no. 5, pp. 1787–1796, 2007.

[36] M. Postma, J. Roelofs, J. Goedhart, T. W. Gadella, A. J. Visser, and P. J. Van Haastert, "Uniform camp stimulation of dictyostelium cells induces localized patches of signal transduction and pseudopodia," *Molecular biology of the cell*, vol. 14, no. 12, pp. 5019–5027, 2003.

[37] C. A. Parent, "Making all the right moves: chemotaxis in neutrophils and dictyostelium," *Current opinion in cell biology*, vol. 16, no. 1, pp. 4–13, 2004.

[38] P. Lu, A. J. Ewald, G. R. Martin, and Z. Werb, "Genetic mosaic analysis reveals fgf receptor 2 function in terminal end buds during mammary gland branching morphogenesis," *Developmental biology*, vol. 321, no. 1, pp. 77–87, 2008.

[39] A. M. Simons, "Many wrongs: the advantage of group navigation," *Trends in ecology & evolution*, vol. 19, no. 9, pp. 453–455, 2004.

[40] L. Coburn, L. Cerone, C. Torney, I. D. Couzin, and Z. Neufeld, "Tactile interactions lead to coherent motion and enhanced chemotaxis of migrating cells," *Physical biology*, vol. 10, no. 4, p. 046002, 2013.

[41] B. A. Camley, J. Zimmermann, H. Levine, and W.-J. Rappel, "Emergent collective chemotaxis without single-cell gradient sensing," *Phys. Rev. Lett.*, vol. 116, p. 098101, Mar 2016. [Online]. Available: http://link.aps.org/doi/10.1103/PhysRevLett.116.098101

[42] R. Mayor and C. Carmona-Fontaine, "Keeping in touch with contact inhibition of locomotion," *Trends in cell biology*, vol. 20, no. 6, pp. 319–328, 2010.

[43] O. J. Maclaren, A. Fletcher, H. Byrne, and P. K. Maini, "Models, measurement and inference in epithelial tissue dynamics," *arXiv preprint arXiv:1506.05052*, 2015.

[44] F. Graner and J. A. Glazier, "Simulation of biological cell sorting using a two-dimensional extended potts model," *Physical review letters*, vol. 69, no. 13, p. 2013, 1992.

[45] M. H. Swat, G. L. Thomas, J. M. Belmonte, A. Shirinifard, D. Hmeljak, and J. A. Glazier, "Multi-scale modeling of tissues using compucell3d," *Methods in cell biology*, vol. 110, p. 325, 2012.

[46] A. F. M. Marée, V. A. Grieneisen, and P. Hogeweg, "The Cellular Potts Model and Biophysical Properties of Cells, Tissues and Morphogenesis," in *Single-Cell-Based Models in Biology and Medicine*, ser. Mathematics and Biosciences in Interaction, A. R. A. Anderson, M. A. J. Chaplain, and K. A. Rejniak, Eds. Birkhäuser Basel, 2007, dOI: 10.1007/978-3-7643-8123-3_5.

[47] K. Torres and S. B. Horwitz, "Mechanisms of taxol-induced cell death are concentration dependent," *Cancer research*, vol. 58, no. 16, pp. 3620–3626, 1998.

[48] R. Grantab, S. Sivananthan, and I. F. Tannock, "The penetration of anticancer drugs through tumor tissue as a function of cellular adhesion and packing density of tumor cells," *Cancer research*, vol. 66, no. 2, pp. 1033–1039, 2006.

[49] Y. Malam, M. Loizidou, and A. M. Seifalian, "Liposomes and nanoparticles: nanosized vehicles for drug delivery in cancer," *Trends in pharmacological sciences*, vol. 30, no. 11, pp. 592–599, 2009.

[50] A. I. Minchinton and I. F. Tannock, "Drug penetration in solid tumours," *Nature Reviews Cancer*, vol. 6, no. 8, pp. 583–592, 2006.

[51] I. K. Kwon, S. C. Lee, B. Han, and K. Park, "Analysis on the current status of targeted drug delivery to tumors," *Journal of Controlled Release*, vol. 164, no. 2, pp. 108–114, 2012.

[52] G. Malet-Engra, W. Yu, A. Oldani, J. Rey-Barroso, N. S. Gov, G. Scita, and L. Dupré, "Collective cell motility promotes chemotactic prowess and resistance to chemorepulsion," *Current Biology*, vol. 25, no. 2, pp. 242–250, 2015.

[53] E. Theveneau, L. Marchant, S. Kuriyama, M. Gull, B. Moepps, M. Parsons, and R. Mayor, "Collective chemotaxis requires contact-dependent cell polarity," *Developmental cell*, vol. 19, no. 1, pp. 39–53, 2010.

[54] E. Scarpa and R. Mayor, "Collective cell migration in development," *J Cell Biol*, vol. 212, no. 2, pp. 143–155, 2016.

[55] A. Szabó and R. Mayor, "Modelling collective cell migration of neural crest," *Current opinion in cell biology*, vol. 42, pp. 22–28, 2016.

[56] J. Varennes and A. Mugler, "Sense and sensitivity: physical limits to multicellular sensing, migration and drug response," *Molecular Pharmaceutics*, 2016.

[57] B. H. Defranco, B. M. Nickel, C. J. Baty, J. S. Martinez, V. L. Gay, V. C. Sandulache, D. J. Hackam, and S. A. Murray, "Migrating cells retain gap junction plaque structure and function," *Cell communication & adhesion*, vol. 15, no. 3, pp. 273–288, 2008.

[58] A. Haeger, K. Wolf, M. M. Zegers, and P. Friedl, "Collective cell migration: guidance principles and hierarchies," *Trends in cell biology*, vol. 25, no. 9, pp. 556–566, 2015.

[59] D. Ramel, X. Wang, C. Laflamme, D. J. Montell, and G. Emery, "Rab11 regulates cell–cell communication during collective cell movements," *Nature cell biology*, vol. 15, no. 3, pp. 317–324, 2013.

[60] H. Gerhardt, M. Golding, M. Fruttiger, C. Ruhrberg, A. Lundkvist, A. Abramsson, M. Jeltsch, C. Mitchell, K. Alitalo, D. Shima *et al.*, "Vegf guides angiogenic sprouting utilizing endothelial tip cell filopodia," *The Journal of cell biology*, vol. 161, no. 6, pp. 1163–1177, 2003.

[61] M. Hsu, T. Andl, G. Li, J. L. Meinkoth, and M. Herlyn, "Cadherin repertoire determines partner-specific gap junctional communication during melanoma progression," *J cell Sci*, vol. 113, no. 9, pp. 1535–1542, 2000.

[62] P. Friedl and D. Gilmour, "Collective cell migration in morphogenesis, regeneration and cancer," *Nature reviews Molecular cell biology*, vol. 10, no. 7, pp. 445–457, 2009.

[63] D. T. Gillespie, "The chemical langevin equation," *The Journal of Chemical Physics*, vol. 113, no. 1, pp. 297–306, 2000.

[64] See https://doi.org/10.5281/zenodo.54980 for source code.

[65] G. B. Ermentrout and L. Edelstein-Keshet, "Cellular automata approaches to biological modeling," *Journal of theoretical Biology*, vol. 160, no. 1, pp. 97–133, 1993.

[66] T. Maire and H. Youk, "Molecular-level tuning of cellular autonomy controls the collective behaviors of cell populations," *Cell systems*, vol. 1, no. 5, pp. 349–360, 2015.

[67] C. Mente, A. Voss-Böhme, and A. Deutsch, "Analysis of individual cell trajectories in lattice-gas cellular automaton models for migrating cell populations," *Bulletin of mathematical biology*, vol. 77, no. 4, pp. 660–697, 2015.

[68] B. A. Camley, J. Zimmermann, H. Levine, and W.-J. Rappel, "Collective signal processing in cluster chemotaxis: roles of adaptation, amplification, and co-attraction in collective guidance," *arXiv preprint arXiv:1512.00544*, 2015.

[69] T. Vicsek, A. Czirók, E. Ben-Jacob, I. Cohen, and O. Shochet, "Novel type of phase transition in a system of self-driven particles," *Physical review letters*, vol. 75, no. 6, p. 1226, 1995.

[70] D. Cai, W. Dai, M. Prasad, J. Luo, N. S. Gov, and D. J. Montell, "Modeling and analysis of collective cell migration in an in vivo three-dimensional environment," *Proceedings of the National Academy of Sciences*, vol. 113, no. 15, pp. E2134–E2141, 2016.

[71] A. Bianco, M. Poukkula, A. Cliffe, J. Mathieu, C. M. Luque, T. A. Fulga, and P. Rørth, "Two distinct modes of guidance signalling during collective migration of border cells," *Nature*, vol. 448, no. 7151, pp. 362–365, 2007.

[72] D. J. Montell, "Morphogenetic cell movements: diversity from modular mechanical properties," *Science*, vol. 322, no. 5907, pp. 1502–1505, 2008.

[73] B. J. Kim, P. Hannanta-Anan, M. Chau, Y. S. Kim, M. A. Swartz, and M. Wu, "Cooperative roles of sdf-1α and egf gradients on tumor cell migration revealed by a robust 3d microfluidic model," *PloS one*, vol. 8, no. 7, p. e68422, 2013.

[74] T. S. Deisboeck and I. D. Couzin, "Collective behavior in cancer cell populations," *Bioessays*, vol. 31, no. 2, pp. 190–197, 2009.

[75] P. Kulesa and S. Fraser, "Neural crest cell dynamics revealed by time-lapse video microscopy of whole embryo chick explant cultures," *Developmental biology*, vol. 204, no. 2, pp. 327–344, 1998.

[76] C. Gaggioli, S. Hooper, C. Hidalgo-Carcedo, R. Grosse, J. F. Marshall, K. Harrington, and E. Sahai, "Fibroblast-led collective invasion of carcinoma cells with differing roles for rhogtpases in leading and following cells," *Nature cell biology*, vol. 9, no. 12, pp. 1392–1400, 2007.

[77] J. Varennes, B. Han, and A. Mugler, "Collective chemotaxis through noisy multicellular gradient sensing," *Biophysical Journal*, vol. 111, no. 3, p. 640, 2016.

[78] N. Bardeesy and R. A. DePinho, "Pancreatic cancer biology and genetics," *Nature Reviews Cancer*, vol. 2, no. 12, pp. 897–909, 2002.

[79] C. W. Gardiner *et al.*, *Handbook of stochastic methods*. Springer Berlin, 1985, vol. 3.

[80] S. Fancher and A. Mugler, "Fundamental limits to collective concentration sensing in cell populations," *Phys. Rev. Lett.*, vol. 118, p. 078101, Feb 2017. [Online]. Available: http://link.aps.org/doi/10.1103/PhysRevLett.118.078101

[81] See Supplemental Information for methods, derivations, and additional discussion.

[82] See https://doi.org/10.5281/zenodo.401040 for source code.

[83] K. Takeda, D. Shao, M. Adler, P. G. Charest, W. F. Loomis, H. Levine, A. Groisman, W.-J. Rappel, and R. A. Firtel, "Incoherent feedforward control governs adaptation of activated ras in a eukaryotic chemotaxis pathway," *Science signaling*, vol. 5, no. 205, p. ra2, 2012.